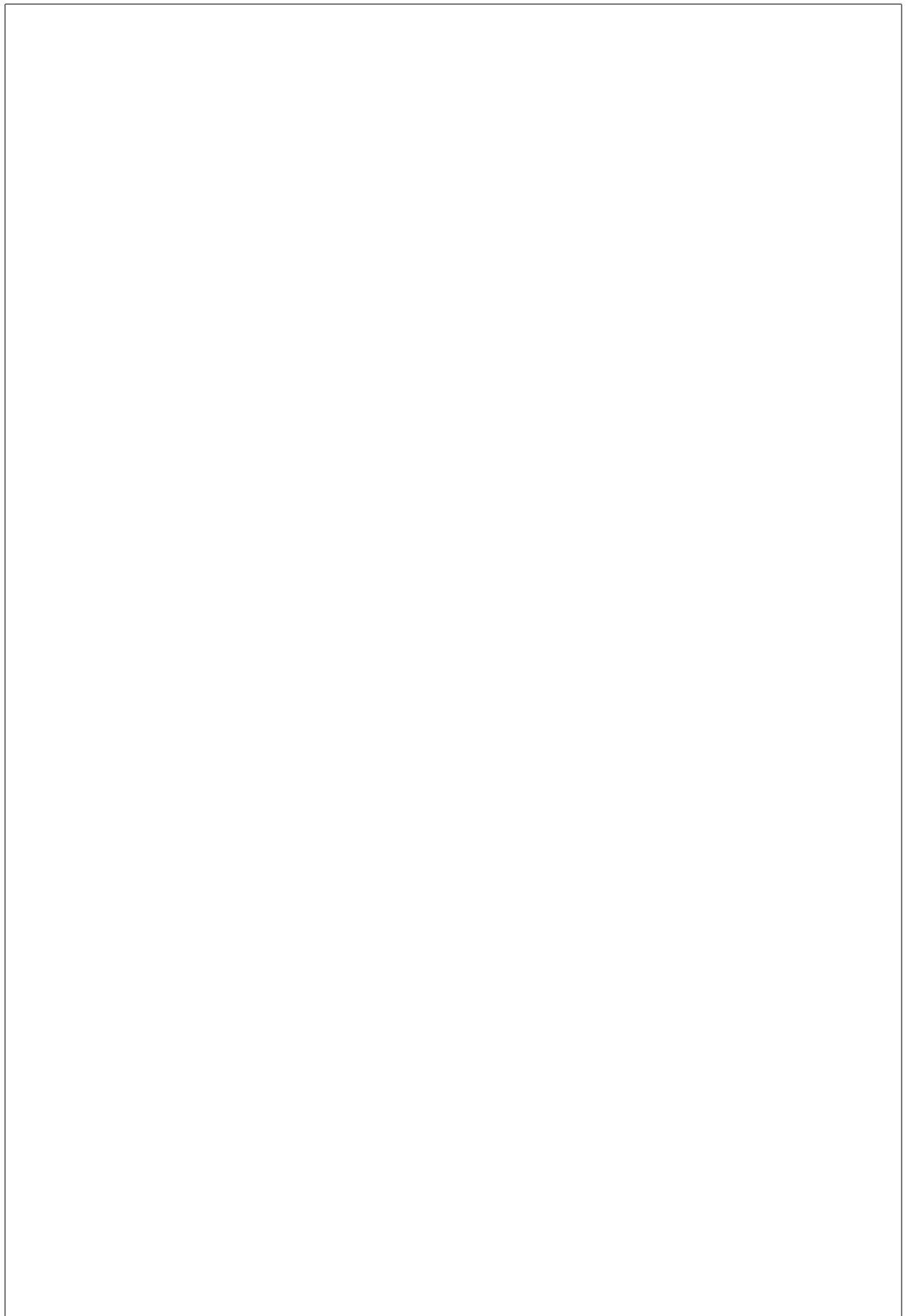


---

---



---

---

---

# Todo list

enter diVincenzo criteria . . . . .	1
Fill in wavelengths used in this thesis and explain why they are used. . . . .	11
saturation already introduced? . . . . .	16
thickness . . . . .	17
value . . . . .	18
value . . . . .	18
short discussion if resolution is enough . . . . .	18
check number . . . . .	18
insert chapter . . . . .	18
specs . . . . .	18
resolution CCD . . . . .	18
optical diffraction, shadows . . . . .	18
type . . . . .	18
fox nachlesen . . . . .	19
wording . . . . .	20
put in reference . . . . .	20
sind die nicht auch zermahlen worden? . . . . .	22
wie kommen da die SiVs rein? . . . . .	22
ueberleitung zu naechstem satz . . . . .	22
is this correct? . . . . .	23
irgendwo einfuegen, was ich diesbezgl. gemacht hab . . . . .	23
put in figure . . . . .	23
info about vibrational mill . . . . .	25
more info . . . . .	25
besser formulieren . . . . .	25
etwas anders fomulieren . . . . .	25
implantation parameters . . . . .	25
how much? . . . . .	27
time? . . . . .	27
check numbers . . . . .	29
sample name . . . . .	29
ist das Wort richtig? . . . . .	31
maybe rephrase . . . . .	31
another citation . . . . .	32
warum . . . . .	32
beginning new text . . . . .	32
end new text . . . . .	32

---

---

type . . . . .	33
check number . . . . .	33
beginning new text . . . . .	34
eher nur vermutung . . . . .	35
end new text . . . . .	35
cite elke . . . . .	36
input Adam Gali . . . . .	41
beginning new . . . . .	41
end new . . . . .	41
beginning new . . . . .	43
correct and verify all numbers . . . . .	43
end new . . . . .	43
think of emitter names . . . . .	46

---

---

---

**Extra long title which spans several lines and therefore  
has to be split manually and the vertical spacing  
has to be adjusted**

**My Name**

**My university**

**(Diploma/doctoral...) Thesis**

**Supervisor:**

**Prof. Dr. Supervisor**  
**Supervisor's Department, University of ...**

**March 2013**

---

---

**Abstract**

A novel method... It is based on...

---

---

---

# Contents

<b>Table of Contents</b>	i
<b>List of Figures</b>	ii
<b>List of Tables</b>	v
<b>Acknowledgements</b>	vi
<b>1 Introduction</b>	1
<b>2 Silicon Vacancy Centers in Diamond</b>	3
2.1 Diamond as a host lattice . . . . .	3
2.2 Classification of diamond . . . . .	4
2.2.1 Classification by impurities . . . . .	4
2.2.2 Classification by crystallinity . . . . .	5
2.3 SiV centers . . . . .	5
2.3.1 Luminescence properties . . . . .	7
2.3.2 Excitation . . . . .	11
2.3.3 Zero phonon line . . . . .	12
2.3.4 Vibrational side-bands . . . . .	12
<b>3 Photoluminescence Setup</b>	16
3.1 Confocal Setup . . . . .	16
3.2 Optical Imaging . . . . .	18
3.3 Spectrometer . . . . .	18
3.4 HBT . . . . .	19
<b>4 Fabrication of Nanodiamonds</b>	21
4.1 HPHT . . . . .	21
4.2 CVD . . . . .	22
4.3 Wet-Milling . . . . .	23
4.3.1 Wet-Milled HPHT Nanodiamonds . . . . .	25
4.3.2 Wet-Milled chemical vapor deposition Nanodiamonds . . . . .	25
4.3.3 Doubly Wet-Milled Implanted Nanodiamonds Implanted With Silicon .	27
4.4 Iridium Substrate . . . . .	29
4.4.1 Preparation of The Substrate . . . . .	30
<b>5 Crystal Quality of Nanodiamonds</b>	31

5.1	Post-Processing Treatments . . . . .	32
5.1.1	Annealing and Oxidation . . . . .	32
5.1.2	Surface Treatment With Gas And Plasma . . . . .	32
5.2	Raman Measurements . . . . .	33
5.3	TEM . . . . .	34
<b>6</b>	<b>Spectral Distribution</b>	<b>36</b>
6.1	Photoluminescence spectra . . . . .	36
6.1.1	Zero-phonon-line . . . . .	40
6.1.2	Sideband . . . . .	41
6.1.3	Cryostatic Measurements . . . . .	43
6.2	$g_2$ Measurements . . . . .	45
6.3	Photostability . . . . .	46
<b>7</b>	<b>discussion</b>	<b>51</b>
<b>8</b>	<b>Conclusion</b>	<b>52</b>
<b>A</b>	<b>Text of Minor Interest</b>	<b>53</b>
<b>Bibliography</b>		<b>54</b>
<b>Index</b>		<b>57</b>

---

---

# List of Figures

2.1	Face-centered cubic diamond lattice . . . . .	3
2.2	Reduced light extraction efficiency of diamond due to refraction . . . . .	4
2.3	Split-vacancy configuration for SiV centers in diamond . . . . .	7
2.4	Band gap of SiV centers hosted in diamond . . . . .	8
2.5	Above-resonant excitation of SiV centers hosted in diamond . . . . .	11
3.1	Confocal setup . . . . .	17
3.2	HBT, spectrometer . . . . .	17
4.1	SEM images of CVD grown diamonds (sample insitucvd) produced by M. Schreck's group (Augsburg University). The average size of these nanodiamonds is 100 nm. (a) Overview image, white dots are nanodiamonds. (b) Detail image, it can be seen that not all nanodiamonds exhibit the same size and that they coexist in different shapes. . . . .	22
4.2	Sketch showing the production of CVD nanodiamonds in the growth chamber with a methane gas environment. . . . .	22
4.3	Pictures of the milled nanodiamonds (sample insitu100). (a) SEM picture showing the distribution of the nanodiamond crystals on the iridium substrate (sample insitu100). (b) Sketch showing the wet-milling process in a vibrational mill. Vibrations from the mill drive the beads which collide with the diamond material and crush it to smaller pieces. . . . .	24
4.4	(a) SEM picture of nanodiamonds sunken into a silicon substrate after annealing at 900 °C for 3 h. Magnification 20 000. (b) SEM image of the microdiamonds after milling on an iridium substrate, but before implantation. In the middle of the picture, there is a reference cross milled into the iridium substrate with a focused ion beam. Its size amounts to 10 µm. It can be seen, that the microdiamonds exhibit sizes of a few micrometer. . . . .	26
4.5	(a) Microscope image of a drop of water on an iridium substrate cleaned with Piranha etch. This picture was used to estimate the contact angle. (b) SEM picture of an 60 nm iridium layer that peeled off the substrate after an ultrasonic bath. . . . .	29
5.1	Raman measurements, black: data, red: fit. (a) Raman measurement before oxidation, sample insitu70. The diamond Raman peak is situated at 1338 cm <sup>-1</sup> . The broad feature around 1600 cm <sup>-1</sup> corresponds to the graphite G-band. (b) Raman measurement after oxidation, sample insitu70o. The G-band has vanished, indicating removal of graphite and amorphous sp <sup>2</sup> hybridized carbon. . .	33

5.2	Transmission electron microscopy (TEM) pictures of sample insitu100. (a) Image of a single nanodiamond particle. Several crystal boundaries can be seen within the diamond particle. (b) Close-up image a diamond particle. The vertical line is a crystal boundary, to the left and right the more or less horizontal layers of one crystalline region can be seen. . . . .	35
6.1	Distribution of the linewidth vs. the center wavelength of the ZPL of the investigated SiV centers in milled nanodiamonds containing <i>in-situ</i> incorporated SiV centers (samples insitu50, insitu70, insitu70n, insitu70o, insitu100). The data can be coarsely separated into two groups, H and V. The cross marks the position of an ideal SiV center in unstrained bulk diamond [1]. The red triangles indicate emitters which exhibited an antibunching dip in the $g^{(2)}(0)$ measurement. Upwards pointing triangles represent emitters which exhibit fluorescence intermittency (blinking), while triangles pointing down represent emitters which do not exhibit any blinking (see section 6.3). The inset displays a zoom into group V, a least squares linear regression to the data, and the 95% confidence interval of the regression as a shaded area around the fit line. A clear trend of broader linewidths for longer ZPL center shifts is visible. . . . .	37
6.2	PL spectra measured with sample insitu100ao. (a) A representative room temperature spectrum of one of the emitters in group H of Figure 6.1, denoted emitter emitter H1. (b) A representative room temperature spectrum of one of the emitters in group V of Figure 6.1, denoted emitter V1. The red lines are Lorentzian fits to the peaks. . . . .	38
6.3	Other representative examples for a) a narrow (denoted emitter H2) and b) a broad (denoted emitter V2) ZPL. In contrast the spectra in Figure 6.2, the emitters depicted here exhibit stronger sidebands. . . . .	38
6.4	Comparison of the distribution of the linewidth vs. the center wavelength of the ZPL of the investigated SiV centers in milled nanodiamonds with data measured on the same nanodiamonds reported by J. Benedikter in [2], with data measured on CVD nanodiamonds, with data measured in CVD diamonds by E. Neu in a filter window between 730 nm and 750 nm [3], and with data measured on implanted250ao, implanted with Silicon. Black symbols represent emitters exhibiting a dip in the $g^{(2)}(0)$ function, indicating a single or very few SiV centers . . . . .	39
6.5	Calculations of the wavelength of the SiV center ZPL in dependence of pressure. Black: hydrostatic pressure; other colors: uniaxial pressure, for different orientations and calculated with different functionals PBE and HSE. Hydrostatic-type pressure causes a moderate blue shift whereas uniaxial strain causes larger redshift with different magnitudes depending on the direction of the strain <b>better description from Adam Gali</b> . . . . .	39
6.6	Shift of dominant sideband peak from the ZPL in spectra of SiV centers (group V, samples insitu50, insitu70, insitu100) vs. ZPL center wavelength. The linear fit shows that the shift decreases with increasing ZPL center wavelength. The shaded area is the 95% confidence interval. . . . .	42
6.7	Representative spectrum of an emitter of group V exhibiting a sideband peak. . . . .	42
6.8	. . . . .	44
6.9	. . . . .	44
6.10	. . . . .	44

6.11 (a) Intensity autocorrelation function of emitter H1 at an excitation power of 15 $\mu\text{W}$ . (b) Intensity autocorrelation function of emitter V1 at an excitation power of 200 $\mu\text{W}$ , which is 25% of the saturation count rate. . . . .	45
6.12 a) The $g^{(2)}$ function of emitter xx at an excitation power of 200 $\mu\text{W}$ , 400 $\mu\text{W}$ and 500 $\mu\text{W}$ from bottom to top. b) Saturation measurement of the same emitter. . . . .	46
6.13 Photon autocorrelation measurement of emitter xx at an excitation power of 500 $\mu\text{W}$ . a) It is evident, that it exhibits a strong bunching. b) In a detail image a small antibunching dip can be seen. While it can be fit with the fitting function of a single emitter, the dip probably does not get fully resolved due to fast dynamics. . . . .	47
6.14 $g^{(2)}(0)$ measurements of emitter xx a) power-dependent, continuous excitation, b) pulsed excitation . . . . .	47
6.15 a) Spectrum of emitter xx b) lifetime measurement of emitter xx . . . . .	48
6.16 Distribution of countrate of a blinking level vs. its retention time in this level. (a) Time trace of the single emitter exhibiting the highest blinking rate. The variation of the countrate in the upper state is attributed to a drift of the setup. (b) Detail of the time trace of the same emitter. . . . .	48
6.17 Retention times of the single emitter exhibiting the highest blinking rate in the bright (red) and dark (blue) states. The dashed line represents a kernel density estimation of the distribution of retention times. The y-axis is scaled to the normalized kernel density estimate. The red solid line is an exponential fit of the bright state retention times, the blue solid line is a lognormal fit of the dark state retention times. The fits are in good agreement with the data (p-values: red 0.92, blue 0.77) . . . . .	49

---

---

# List of Tables

2.1	Classification of diamond synthesized by chemical vapor deposition . . . . .	6
4.1	Summary of the samples grown on diamondoid seed crystals. . . . .	24
4.2	Summary of the wet-milled samples. The first column indicates the names of the samples, the second the mean diameter of the nanodiamonds, and the third describes how the silicon was incorporated into the diamond. . . . .	28

---

---

# Acknowledgements

First of all, I want to thank my supervisor...

I am very grateful for the guiding help of...

I am grateful to...

---

---

# Chapter 1

## Introduction

“Every competent physicist can ‘do’ quantum mechanics, but the stories we tell ourselves about what we are doing are as various as the tales of Sheherazade, and almost as implausible.” - David J. Griffiths

Quantum optics is the sciences of light which deals with single light particles, namely photons. Within the last few years the topic of quantum technologies has witnessed a large progress in fields like quantum cryptography, quantum computation and quantum metrology. Requirements for these technologies are ideally single photons which are produced “on demand” i.e. deterministically and have well defined properties. For instance, quantum computing places restraints on the photon sources, called the diVincenzo criteria (). The progress of these technologies calls for measurement standards to make the individual measurements comparable???. The candela is the SI (système internationale) unit for optical radiation [4] and is the only unit which is linked to physiological processes, namely the varying sensitivity of the human eye to radiation of different frequencies. It is a photometric quantity, meaning that a physical measurement of the light in terms of luminous intensity represents the visual sensation experienced by a human observer exposed to the same source of light. It is one of the base units since the system was first introduced. In the latest definition, the candela is linked to the unit watt. The current definition of the candela (cd) is the following: “The candela is the luminous intensity, in a given direction, of a source that emits monochromatic radiation of frequency  $540 \times 10^{12}$  hertz and that has a radiant intensity in that direction of  $1/683$  watt per steradian.”[5] Advances in the quantum technologies which operate in the photon-counting regime would profit from a redefinition of the candela in terms of photon number, named “quantum candela”.

The term “quantum candela” is used to describe a reformulation of the candela by defining it via a countable number of photons. This new definition would be of a form that converts the current definition into

$$P = nh\nu \quad (1.1)$$

where

enter di-Vincenzo criteria

$P$  = power =  $1/683$  W exactly

$n$  = number of photons per second

$h$  = Planck's constant =  $6.626\,069\,3(110000000) \times 10^{-34}$  J s

$\nu$  = photon frequency =  $540 \times 10^{12}$  Hz exactly

which yields [4]

$$n = 4.091\,942\,9(70000000) \times 10^{15} \text{ s}^{-1}$$

The number of photons of all wavelengths emitted or contained in a given beam of light is given by [6]:

$$N_P = \int \frac{E_\nu}{h\nu} d\nu = \int \frac{\lambda E_\lambda}{hc} d\lambda \quad (1.2)$$

From this equation, the minimal number of photons to illuminate a scene can be calculated. However, in nature most light sources emit continuous light, therefore not the absolute number of photons, but the number of photons emitted per unit time, i.e. the photon flux  $\Phi_P$  is of interest:

$$\Phi_P = \frac{dN_P}{dt} \quad (1.3)$$

For high-accuracy absolute radiometry at the quantum level, predictable or quasi-single-photon sources and photon detectors are needed. A key requirement for the progress of quantum information technology is the development of sources that deterministically produce single photons upon request (on-demand source). Colour centres in synthetic diamond represent an interesting single-photon source with strong anti-bunching and a spectral width about 1nm at room temperature [6]. Being a solid state system, they are easy to handle and neither cooling nor vacuum is required. Diamond has the advantage, that it is a homogeneous host material, therefore the color center can be treated as a single atom. Additionally, it has a large band gap of 5.5 eV [7] Why nanodiamond? higher extraction efficiency of fluorescence light easy positioning using pick-and-place technique easy to obtain isolated color centers Why silicon-vacancy center? bright single photon source (count rates up to Mcps) narrow linewidth of zero-phonon line (down to 0.7 nm at room temperature) For the application of silicon vacancy color centers as absolute single-photon sources a fully characterized state of the emitted light is imperative.

---

---

## Chapter 2

# Silicon Vacancy Centers in Diamond

### Remark:

- Fill in used energies for SiV center excitation.

## 2.1 Diamond as a host lattice

Diamond is a metastable modification of carbon which is, in fact, stable under normal conditions [?]. Carbon atoms form strong  $sp^3$ -bonds with each other in a tetraedral arrangement of neighboring atoms. The resulting  $sp^3$ -hybridized lattice is of exceptional mechanical stability, making diamond the hardest known material [?]. The crystal structure can also be interpreted as a face-centered cubic (fcc) lattice with two carbon atoms in the primitive Bravais cell, situated at  $(0, 0, 0)$   $a$  and  $(\frac{1}{4}, \frac{1}{4}, \frac{1}{4})$   $a$  with  $a = 3.567 \text{ \AA}$  denoting the lattice constant [?]. Figure 2.1 illustrates the structure.

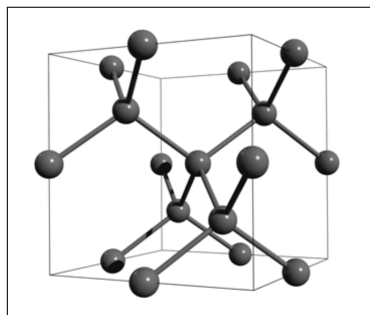


Figure 2.1: Face-centered cubic diamond lattice. Note the tetraedral arrangements of carbon atoms. Figure reproduced with permission from [?].

The valence and conduction bands of diamond are separated energetically by a large direct band gap of 7.3 eV while its indirect band gap amounts to 5.5 eV [?, ?]. As a result diamonds are transparent for light of all wavelengths larger than 230 nm [?]. This transparent quality makes diamond an ideal host material for various optically active lattice defects or impurities. These induce a wide range of discrete energy levels accommodated by the sizable band gap. The absorption of optically active impurities or impurity complexes gives rise to the color of

diamonds, thus these impurities are commonly termed color centers [?]. Due to the exceptional mechanical stability of diamond color centers too are very stable, another important property enabling optical applications.

A property of diamond, detrimental to some optical applications, is its large refractive index with values of 2.49 at 360 nm and 2.4 at 800 nm respectively [?]. Thus, a portion of the fluorescent light escaping from the diamond is reflected back into it, effectively reducing the efficiency of light extraction. If nanodiamonds smaller than the wavelength of the light to be collected are used, internal reflection is suppressed and the extraction efficiency can be increased [?].

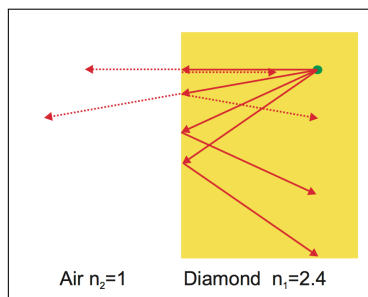


Figure 2.2: Light from a fluorescent emitter inside the diamond (green dot) undergoes reflection at the diamond-air interface. Figure reproduced with permission from [?].

## 2.2 Classification of diamond

Two major approaches for classifying diamond are commonly encountered. First, classification according to the presence or absence of certain impurities or impurity complexes. Second, classification based on different diamond crystallinities observed. In the following both classification systems are briefly introduced.

### 2.2.1 Classification by impurities

Impurities or complexes of impurities in the diamond lattice can be optically active and thus change the optical properties of diamond. Most strikingly perhaps is the appearance of color in otherwise colorless diamond due to a sufficient concentration of such defects. Using IR absorption spectroscopy the degree of nitrogen impurities can be determined. It is used to subdivide diamonds into distinct groups named Type I and Type II [?, ?]. The groups are further subdivided as follows:

- Type Ia: With a nitrogen concentration of up to 3000 ppm most natural occurring diamonds belong to this group [?]. Nitrogen appears arranged predominantly in aggregate clusters forming complexes of impurities. These complexes are optically active, absorbing light in the blue range of the visible spectrum. Consequently Type Ia diamonds often exhibit a yellow to brownish coloration.
- Type Ib: With concentrations of up to 500 ppm nitrogen atoms appear predominantly in isolation, replacing individual carbon atoms in the diamond lattice. In addition to

absorbing visible blue light, green is being absorbed as well. Type Ib diamond thus exhibits intensified the yellow or brownish coloration. While only 0.1 % of naturally occurring diamond fall into this class, almost all synthetic diamonds created using the high-pressure, high-temperature (HPHT) method are of Type Ib [?].

While Type I diamond exhibits an appreciable concentration of nitrogen, Type II diamonds lack nitrogen entirely. Type II diamond is divided into two subgroups according to the presence or absence of boron as follows:

- Type IIa: Can be considered pure as they lack boron impurities and other optically active defects [?]. They thus are colorless. Up to 2 % of naturally occurring diamond and most diamonds synthetically created using the chemical vapor deposition (CVD) method are of Type IIa [?].
- Type IIb: Contains appreciable concentrations of boron atoms replacing individual carbon atoms in the diamond lattice. Boron defects are optically active absorbing visible light ranging from red to yellow. Depending on the Boron concentration blue to grey colorations are observed. Furthermore, diamond is turned from an insulator to a efficient p-type semiconductor in the presence of boron impurities [?].

We remark that for many modern applications of diamonds the presented "classic" categorisation of diamond is not enough. In these cases a precise quantification of the concentration and nature of various relevant impurities is called for [?, ?].

In this section we also briefly touched upon the CVD and HPHT methods, two approaches to synthetically produce diamonds. Both are relevant for this thesis and are explained in detail in chapter 4.

### 2.2.2 Classification by crystallinity

Up until now, the discussion assumed that diamond forms a lattice consisting of one giant single crystal. However, other crystallinities are possible and can be used to classify diamond. They range from mono or single crystals to polycrystalline, nanocrystalline or even ultra-nanocrystalline diamond films [?]. This classification is particularly useful for synthesized diamond as will be discussed in chapter 4. Table 2.1 summarizes the different sizes of diamonds or diamond films which can be achieved using variations of the CVD method.

Diamond films consist of isolated diamond grain of random orientation with sp<sup>2</sup> hybridized grain boundaries and graphit-like inclusions [?]. Carbon present in non-diamond phases, e.g. graphite or amorphous carbon gives rise to detrimental light absorption while crystal boundaries lead to increased scattering losses. As the size of diamond crystallites get smaller, the ratio of non-diamond carbon to diamond carbon increases. Thus losses are most pronounced for the smallest grain diamond films.

## 2.3 SiV centers

A color center is an optically active point-defect in a crystall lattice, capable of absorbing and emitting light. Defects can consist of one or several vacant lattice sites, foreign atoms replacing lattice atoms or a combination thereof. If the presence of a defect induces discrete

Table 2.1: Classification of diamonds synthesized using CVD [?].

Crystallinity	Grain size
monocrystalline	arbitrary
polycrystalline	50 nm to 10 $\mu\text{m}$
nanocrystalline	10 nm to 50 nm
ultra-nanocrystalline	< 10 nm

energy levels located in the band gap of the host material, the color center can be interpreted as its own quantum system. In other words, the color center can be viewed as a single isolated and localized artificial atom embedded in a host matrix. As such it is able to absorb light and emit single photons by means of fluorescence.

Compared to alternative single photon sources like single atoms [?], Ions [?] or individual quantum dots [?, ?], color centers offer a couple of advantages due to their solid state environment. As a result of the high mechanical stability of the host lattice color centers exhibit increased photo-stability, in particular compared to organic molecules as light sources. Furthermore the host lattices offers protection for color centers from detrimental interactions with aggressive free molecules [?]. Lastly, color centers can be handled and investigated at room temperature, thus significantly reducing the experimental efforts necessary to study them.

Of particular interest are color centers as single photon sources when hosted in diamond. With its transparency, exceptional stability and minimal phononic interactions at room temperature the diamond lattice is an ideal host matrix for color centers [?, ?]. While more than 500 different color centers in diamond are documented, only a small fraction has been investigated with respect to their properties as single photon sources [?]. For an in-depth review of color centers and their versatile applications see [?, ?]. The two arguably most prominent examples of well-studied color centers are vacancy centers featuring nitrogen and silicon [?, ?, ?].

The silicon-vacancy (SiV) center in diamond and its properties is at the center of this thesis. The SiV center has been established as an efficient single photon source at room temperature. It shows very narrow emission lines with record count rates up to  $6.2 \times 10^6$  cps (counts-per-second) [?]. The emission of indistinguishable photons and the optical access of electronic spin states have been demonstrated [?, ?, ?, ?], hinting at the possibility of deploying SiV centers as spin-qubits.

A silicon-vacancy center is formed in a diamond lattice by substituting two carbon atoms by a silicon atom and a nearby empty lattice site respectively. The silicon atom occupies its energetically optimal position by sitting in-between two lattice sites. This is called “split-vacancy” configuration and induces a  $D_{3d}$  symmetry with the two vacancies and the impurity aligned along the  $\langle 111 \rangle$  diamond axis [?], see Figure 2.3.

The SiV center is known to occur in two different charge states. The first is the neutral state or  $\text{SiV}^0$  with a zero-phonon transition at 1.31 eV (946 nm). It is associated with a  $S = 1$  ground state [?]. The second state is the negatively charged state  $\text{SiV}^-$  where the silicon-vacancy center recruited an additional free electron. It exhibits a zero-phonon transition at 1.68 eV (738 nm). Its ground state has been determined as a  $S = \frac{1}{2}$  state [?, ?]. Due to its outstanding brightness and the location of the zero-phonon-line in the visible range of the spectrum, this thesis focuses on the negatively charged SiV center. For convenience we drop

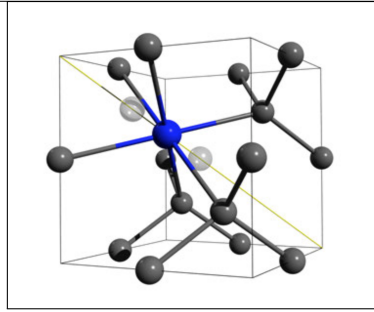


Figure 2.3: Crystal structure of the SiV center embedded into the diamond lattice: The silicon atom (blue sphere) sits in between two vacant lattice sites (white spheres) forming a “split-vacancy” configuration aligned along the  $\langle 111 \rangle$  crystallographic axis (yellow line). Figure reproduced with permission from [?].

the charge distinction from now on and refer to  $\text{SiV}^-$  centers simply as SiV centers.

SiV centers have been created using CVD in nanodiamonds and single-crystal diamond films [?], see chapter 4 for details. It is also possible to directly implant silicon atoms into pure diamond. High temperature annealing must then be used to animate present lattice vacancies to recombine with silicon impurities in order to form split-vacancy SiV centers [?, ?].

In the following sections we detail the most important luminescence properties of SiV centers in diamond. For a comprehensive review we refer to [?, ?] and references therein.

### 2.3.1 Luminescence properties

The silicon-vacancy center as a quasi-atomic system is capable of absorbing and emitting light. When a ground state electron absorbs a photon of appropriate energy, it is promoted to a discrete higher-energy excited state located within the band gap of the diamond host matrix. Reversing this excitation relaxes the electron back down to the ground state while emitting a so-called fluorescent photon, accounting for the energy difference between excited and ground state. This transition is “spin-allowed”, limiting the life-times of excited states to nano-seconds and thus promoting rapid relaxation and associated fluorescence [?].

Since fluorescence is directly linked to the electronic structure of the SiV center, see Figure 2.5. It follows that photoluminescence spectroscopy can be used to study it using a laser to optically excite the SiV center. In the context of this thesis, optical above-resonant excitation is the method of choice, in particular, when used in conjunction with a confocal photoluminescence setup which will be discussed in chapter 3. If the excitation energy exceeds the energy of the lowest excited state, electrons are promoted to higher electronic and vibrational states. Conveniently, these states relax rapidly towards the lowest excited state in non-radiative processes [?]. Once the lowest excited state is reached, a fluorescent transition can follow. It has been shown that above-resonant excitation is feasible for excitation energies ranging from 1.75 eV to 2.55 eV [?, ?, ?]. If the excitation energy is chosen too high, however, the SiV center is ionized. Electrons donated to the diamond conduction band do not participate in fluorescence. Ionization may be reversed if a positively charged SiV center manages to capture a free electron from the conduction band. This charge state conversion is believed to be linked to fluorescence intermittence, more intuitively named as blinking SiV centers [?, ?].

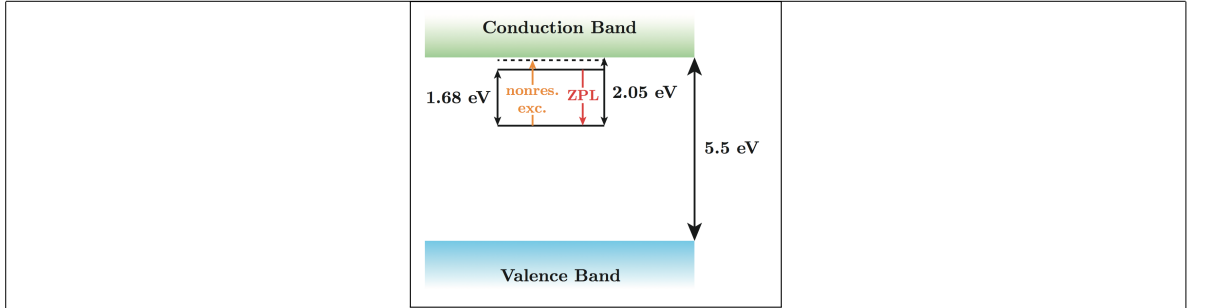


Figure 2.4: Simplified picture of the generous 5.5 eV band gap of diamond with discrete states induced by the presence of SiV centers. The SiV center ground state is situated 2.05 eV below the diamond conduction band. The lowest excited state sits 1.68 eV above the ground state with the zero-phonon-line transition in red connecting the two. Above-resonant optical excitation is indicated in orange. Figure courtesy of [?].

The fluorescence spectrum of SiV centers have two prominent features: A narrow zero-phonon-line and a broad phonon side band. The former is connected to fluorescent photons associated with a purely electronic transition while the latter involves vibrational transitions involving electron-phonon interactions. The phonon side band is typically shifted to higher wavelengths with respect to the zero-phonon-line. The resulting energy deficit can be explained by phonons being created during the relaxation of higher vibrational states. A shift in the opposite direction can also be observed in rare cases if phonons are absorbed during the relaxation process [?].

The relative strength of the zero-phonon-line and the phonon side band is connected to the electron-phonon coupling of the excited color center and thus to lattice vibrations. When a color center is excited, its charge distribution changes. As a result, the equilibrium positions of all particles involved in the color center shift leading to changes in color center geometry. Naturally, the combined changes of charge distribution and geometry of the color center affect the surrounding atoms of the host lattice. Similarly, if the exited state relaxes back to the ground state, the process occurs in reverse. Thus, due to differing atomic arrangements for ground and exited states, the emmission and absorption of photons is accompanied by lattice vibrations, i.e. phonons [?].

The Huang-Rhys model allows us to discuss the electron-phonon interaction in more detail. Our discussion follows the presentation in [?]. The model assumes in its simplest form that vibrational modes can be modelled as oscillations of nuclei between their euqilibrium coordinates  $q$  associated with the electronic states [?]. Let  $\mathcal{K}_{3A_2}$  and  $\mathcal{K}_3E$  denote the harmonic potentials of the ground and excited states respectively:

$$\mathcal{K}_{3A_2} = \frac{1}{2}\Omega^2 q^2 \quad (2.1)$$

$$\mathcal{K}_3E = C_3E + aq + \frac{1}{2}(\Omega^2 + b)q^2 \quad (2.2)$$

$$= C_3E - C_R + \frac{1}{2}(\Omega^2 + b)(q - \delta q)^2. \quad (2.3)$$

It follows that the vibrational modes of ground and exited states are given as harmonic states

with discrete energies  $\hbar\Omega(\nu + 2)$  as well as  $\hbar\sqrt{\Omega + b}(\nu + 2)$  respectively, where  $\nu$  denotes the occupation number and  $\Omega$  the frequency. Further,  $aq$  denotes the linear nuclear displacement of the excited state configuration with respect to the ground state equilibrium where  $q = 0$ . The quadratic term  $bq^2$  refers to the vibrational frequency shift due to a redistribution of charge between the electronic states. From the linear and quadratic coupling strengths  $a$  and  $b$ , the equilibrium displacement of the  $^3E$  state is given by:

$$\delta q = \frac{-a}{\Omega^2 + b}, \quad (2.4)$$

while the relaxation energy reads [?]:

$$C_R = \frac{a^2}{2(\Omega + b)} = \hbar S \sqrt{\Omega + b}, \quad (2.5)$$

where  $S$  is referred to as Huang-Rhys factor.

The harmonic potentials and states are schematically shown in figure 3.6, with the excited state potential being shifted by the equilibrium displacement  $\delta q$  with respect to the ground state potential.

Applying the Franck-Condon principle, the most probable electronic transition from the excited  $3E$  state to the ground state  $3A2$  originates from the fundamental vibrational  $3E$  state at  $\delta q$  into higher vibrational levels of the  $3A2$  ground state followed by non- radiative relaxation to the fundamental  $3A2$  vibrational level that effectively displaces the nuclei to the ground state equilibrium coordinate. The excitation from  $3A2$  to  $3E$  proceeds vice versa. The Huang-Rhys factor  $S$  physically describes the mean number of vibrational quanta involved in the optical transition. For the NV center, the Huang- Rhys factor is typically  $S = 3.76$  and the energy of the ground state vibrational mode is  $\hbar\omega_0 = 65$  meV [168, 214]. The most probable transition originating from  $\delta q$  marks the maximum in the emission spectrum at  $\lambda_{max} = \hbar\omega_0/2\pi = 650$  nm, shifted to longer wavelengths with respect to the ZPL. Other transitions are less probable and less intense. For the NV center, we expect maximum intensity at 1.7eV (728nm). In absorption, an excitation energy of  $\hbar\omega_0 = \hbar\omega_{ZPL} + S\hbar\omega_0 = 2.19$  eV (565 nm) efficiently excites the NV center, which corresponds well with the 532nm excitation wavelength widely used for off resonant excitation. A second measure of the electronic-vibrational coupling is the Debye-Waller factor  $D_w$ , which is related to the Huang-Rhys factor via  $D_w = \exp(-S)$ . The Debye-Waller factor determines the ratio of photons emitted into the zero-phonon line compared to the overall emission. Due to the poor ZPL branching ratio, the Debye-Waller factor of the NV center amounts only  $D_w = 2$ .

The energy of the excited state in the case of electron phonon coupling can be written as [37]:  $V_e = E_e + 1/2\hbar\omega_0^2 q^2 + aq + bq^2$  (2.1) Here, the term  $E_e$  corresponds to the electronic energy of the excited state, whereas the term  $1/2\hbar\omega_0^2 q^2$  corresponds to the vibrational energy of the state (potential approximated as being harmonic). The following two terms account for the linear electron-phonon coupling  $aq$  and the quadratic coupling  $bq^2$ , with  $q$  being the displacement of the nuclei from their equilibrium positions. The linear coupling term corresponds to a constant change in the positions of the atomic nuclei between the ground and the excited state whereas the quadratic coupling describes a change in the vibrational frequencies. For the understanding of the PSB, the linear electron-phonon coupling has to

be considered in greater detail. In Fig. 2 (b) the vibrational parabolas of an electronic ground and an excited state are shown for an arbitrary value of  $q$ . Since the excitation process (orange arrow) is very fast, it occurs vertically in terms of  $q$ , which means, that the system is excited into a higher lying vibrational state of the excited electronic state. The excitation occurs to the vibrational state with the wavefunction that has the largest overlap with the wavefunction of the initial state. Subsequently, on a larger time scale, the nuclei react on the changed charge distribution and relax in their new equilibrium positions. The excited vibrational state then relaxes into the vibrational ground state (dashed arrow) of the electronic excited state by non-radiative internal conversion processes. The following electronic relaxation process (red arrow) is again much faster than the movement of the atomic nuclei and the system will again end up in a vibrational excited state of the electronic ground state. Again, the final state which has the largest overlap with the vibrational ground state of the electronic excited state has the highest probability [38]. From Fig. 2 (b) it is easily noticeable that the value of  $q$ , which means the amount the parabolas are shifted against each other, determines the most probable vibrational state the system relaxes to. This probability is usually expressed by the so called Huang-Rhys factor  $S$ , which is given by  $2 \neq \hat{S} |M_{0n}| = S n!$  (2.2) with  $|M_{0n}|^2$  being the intensity of the transition to the  $n$ th vibrational excited state [37]. If  $S$  equals two, this means, that the most probable vibrational state the system relaxes to, is the state with  $n=2$ . This case is illustrated in Fig. 2 (b). For  $S$  approaching zero, the most probable transition becomes the zero phonon line, which means, that the ratio of the ZPL fluorescence to the total fluorescence in the spectrum is given by  $I_{ZPL} = e \hat{S}$ . (2.3) IZP L+P SB The Huang-Rhys factor of the SiV centre has been determined to amount to  $S=0.08$  up to  $S=0.24$  [39, 40, 41]. This means that the major part of the fluorescence of the SiV centre is concentrated in its zero phonon line making it a very narrowband single photon source (even for  $S=0.24$  only around 23A transition at 1.681eV in the spectrum has been assigned to the negatively charged SiV centre [42, 43] whereas a transition at 1.31 eV has been attributed to the neutral charge state [44]. However, since the fluorescence of the neutral SiV charge state is usually relatively weak the interest focusses on the bright 1.681 eV transition of the negatively charged centre. If SiV centres are cooled below approximately 110 K, the ZPL splits into several fine structure components [45]. As seen in Fig. 3 (a), in large ensembles of SiV centres, up to twelve different lines can be observed with intensities corresponding to the natural abundances of the three stable isotopes of silicon. Each isotope contributes with four lines to the total spectrum. The lines are labelled with A1 to D1 etc. starting with the line of highest energy. As shown in Fig. 3 (b), in a spectrum of a single SiV centre this four-line fine structure is more obvious. The distribution of the fluorescence intensity over the four lines shown for this emitter is characteristic for a SiV centre in bulk diamond exhibiting only a small local crystal strain. This rather unique pattern unveils, together with temperature-dependent photoluminescence measurements, that the electronic structure of the centre has to contain two levels in the ground and the excited state, with a splitting of around 0.02 meV and 1.07 meV, respectively[43]. In the following chapters, this splitting pattern will be a starting point to get more detailed information about the electronic structure as well as the symmetry properties of the negatively charged SiV centre.

### 2.3.2 Excitation

To observe single photons being emitted from SiV centers hosted in diamond, color centers first need to be excited. In the context of this thesis, optical above-resonant excitation is the

method of choice, in particular, when used in conjunction with a confocal photoluminescence setup, see chapter 3.

It is known that above-resonant excitation of SiV centers is feasible for excitation energies ranging from 1.75 eV to 2.55 eV [?].

For SiV centers it is known that above-resonant excitation promotes electrons to states below the edge of the conduction band of the diamond host as long as excitation energies do not exceed 2.05 eV [?].

Using an excitation laser with a wavelength above the fluorescent wavelength of SiV centers causes electrons to be promoted from the ground state to excited states with energy levels exceeding the energy of the lowest excited state. Conveniently, the dissipative nature of the silicon-vacancy center is such that electrons in higher excited states quickly relax down to the lowest excited state in a non-radiative process. From there electrons may relax further down to the ground state, emitting observable single fluorescent photons. Figure 2.5 illustrates the process. We remark that possible shelving states exhibiting both radiative and non-radiative dissipation are believed to be involved in the SiV center relaxation processes [?]. While we omit a discussion of these states and their implications here, the interested reader is referred to [?] and references therein for a detailed description of the electronic (fine)structure of SiV centers.

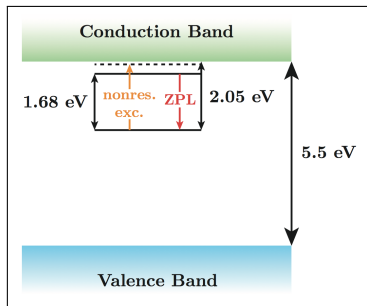


Figure 2.5: Simplified picture of above-resonant optical excitation of SiV centers in nanodiamonds [?].

To verify whether a SiV center can be optically excited, transitions of the SiV center can be observed using direct absorption [?, ?]. Alternatively photoluminescence excitation spectroscopy may be used to investigate the fluorescence intensity of color centers as a function of different excitation wavelengths. Using this method it has been shown that SiV centers can be excited (with varying efficiency) over a broad spectral range between 1.75 eV to 2.55 eV [?, ?].

In this work we will use the following excitation energies.

### 2.3.3 Zero phonon line

Generally, the purely electronic transition of a color center, the zero-phonon-line (ZPL), is the spectrally narrowest transition of the color center. In contrast, vibration assisted electronic transitions (vibronic sidebands) are much broader. Thus, to enable low bandwidth single photon emission, a color center's fluorescence should concentrate into a narrow ZPL. The SiV center is a promising candidate for such a low bandwidth emitter as discussed in the

Fill in  
wave-  
lengths  
used in  
this the-  
sis and  
explain  
why they  
are used.

following sections. Previous reports in the literature often reflect the luminescence properties of (large) ensembles of SiV centers. Feng et al. [139] report a linewidth of 15meV (6.5nm) for an ensemble of SiV centers in polycrystalline diamond (PCD). Gorokhovsky et al. [112] specify 13.6 meV (6 nm) in the same material system. More recently, Vlasov et al. [132] find a width of 7 nm for SiV centers in PCD and 8 nm for ultrananocrystalline diamond. In highly stressed low quality PCD, the ZPL of the SiV center might be split and broadened to span the wavelength range of 733 Å– 745 nm [96]. Thus, several reports indicate that the ZPL of the SiV centers may be sufficiently narrow to enable low bandwidth single photon emission. The spread of linewidths observed in these reports indicates that the linewidth of SiV ensembles is influenced by inhomogeneous broadening. The significant influence of inhomogeneous broadening becomes especially visible in low temperature spectra, where the homogenous broadening due to phonons that dominates at room temperature is strongly reduced and only the linewidth due to inhomogeneous broadening remains. A detailed discussion of the line broadening mechanisms for the ZPL is presented in Sec. 7.2.1. Feng et al. [139] measure a linewidth of 10meV (4.4nm) at 10K. Clark et al. [140] find a width of 16.8meV (7.4nm) at 77K, with a reduction to 8.4meV (3.7nm) after an HPHT annealing step. The major source for the inhomogeneous broadening is mechanical stress in the diamond [96]. A detailed discussion of the sources of stress in the samples employed in this work can be found in Sec. 5.2.1. Only two reports of the linewidth of single centers exist: Wang et al. report a ZPL linewidth of 5 nm [37] and 6 Å– 1 nm [74] at room temperature. We point out that in the work of Wang [74] also centers with significantly lower linewidth have been observed: A center with an emission wavelength of 736.8 nm and 1.3 nm ZPL width is not identified as an SiV center due to the short emission wavelength. Nevertheless, this blue shift of the ZPL might be due to the crystalline environment in the vicinity of the center: As mentioned above, reports in the literature clearly indicate inhomogeneous broadening of the ZPLs of ensembles of SiV centers in the nm range. Thus, one expects line positions spread over the inhomogeneous linewidth when observing single emitters and a ZPL observed at 736.8 nm might be due to an SiV center. At low temperature, in diamond with a low inhomogeneous broadening of the ZPL, a four line fine structure of the ZPL transition has been observed [111,140]. This specific line pattern might be considered as the “spectral fingerprint” of the SiV center and might be used to prove the identification of single color centers as SiV centers. A detailed discussion of the pattern as well as the associated level scheme is performed in Sec. 7.1. Together with a narrowing of the line upon cooling and the occurrence of the four line pattern, the SiV ZPL blue shifts 1.2-1.4nm upon cooling [112,139].

### 2.3.4 Vibrational side-bands

The linear electron-phonon coupling of the SiV center will be discussed in the following, while further discussion of quadratic electron-phonon coupling is shifted to section 7.2.2, where it is used to interpret temperature dependent spectra of single SiV centers. Vibronic sidebands in emission mostly occur as transitions from the vibrational ground state ( $n = 0$ ) of the excited electronic state to higher vibrational states ( $n > 0$ ) of the electronic ground state (for the level scheme see Fig. 1.6). Consequently, these lines are red shifted compared to the ZPL in luminescence. The red shift gives the phonon energy of the corresponding phonon mode if  $n = 1$  (one-phonon sideband). For higher order sidebands ( $n > 1$ ), the energy is a multiple of the phonon energy. In absorption, sidebands are blue shifted compared to the ZPL. Here, absorption mostly takes places from the vibrational ground state ( $n = 0$ , highest population)

in the electronic ground state to higher vibrational states ( $n \geq 1$ ) in the excited electronic state. The sideband spectrum together with the ZPL is characteristic for a specific color center [25], assisting to identify the emitting centers. The vibronic sidebands of the SiV center are weak compared to the ZPL even at room temperature. This indicates a weak linear electron-phonon coupling and renders SiV centers especially suitable as low bandwidth emitters. The linear electron-phonon coupling is measured either by the Debye-Waller factor (DW) or the Huang-Rhys factor (S). The Debye-Waller factor is defined as the integrated luminescence intensity of the ZPL  $I_{ZPL}$  divided by the integrated luminescence intensity of the color center  $I_{tot}$  [27]. The Huang-Rhys factor S is defined by  $I_{ZPL} = \exp(-S)$  [84].  $I_{tot}$  The Huang-Rhys factor can be interpreted as an indication of the most probable (vibration assisted) transition (discussion following Ref. [84]). Figure 1.6 indicates the situation for a Huang-Rhys factor S close to zero and for S = 2. For a very low Huang-Rhys factor, the most probable transition is the ZPL, it dominates the luminescence spectrum. For a Huang-Rhys factor of S = 2, the most probable absorption transition brings the color center to the vibrational state with  $n = S = 2$  phonons in the excited electronic state. This transitions marks the maximum of the absorption band. Subsequently, the color center relaxes the excess energy of  $n = S$  phonons in the excited state. The most probable luminescence transition then brings the color center to the vibrational state with  $n = S$  phonons in the ground state. This transition marks the maximum of the emission band. The intensity  $|M_{0n}|^2$  of the vibronic sideband involving n phonons is given by [94]  $2^n e^{-S} |M_{0n}|^2 = S^n n!$ . (1.5) In the literature, measurements on SiV center ensembles have been used to determine the Huang-Rhys factor S: Rossi et al. [136] report S = 0.1 deduced from luminescence measurements at room temperature using 457 nm excitation. Gorokhovsky et al. [112] report S = 0.08 also deduced from luminescence measurements at 9 K using 515 nm excitation. Collins et al. [118] report S = 0.24 ± 0.02 in absorption at room temperature. These experiments have been performed using polycrystalline CVD diamond grown on Si substrates. We point out that different spectral ranges have been investigated in the publications mentioned above: Ref. [136] discusses spectra ranging down to 1.4 eV, while Ref. [112] gives spectra only down to 1.59 eV for 515 nm excitation. In Ref. [118], absorption spectra with energies up to 1.78 eV are used. Due to the restricted spectral ranges investigated, the question whether all possible sidebands have been taken into account might be raised (for a discussion of sideband energies of the SiV center see below). Additionally, in Ref. [136] a background subtraction is performed before S is calculated from the luminescence spectrum, while this is not discussed in Refs. [112] and [118]. Furthermore, the authors of Refs. [112, 118, 136] do not discuss whether the employed data has been corrected for a varying detection efficiency of the experimental setup throughout the investigated spectral range. Considering these experimental issues, it is not clear which of the values most closely describes the linear electron-phonon coupling of the SiV center and how the values compare to each other. Assuming a Huang-Rhys factor of S = 0.24, the relative intensities compared to the ZPL are 24% for the one-phonon sidebands and only 2.8% for the two-phonon sideband. Thus, the ZPL dominates the spectrum. Additionally, one would not expect to observe sidebands related to two-phonon processes for SiV centers. These findings are in accordance with reports in the literature that in general color centers involving heavier impurities tend to exhibit low linear electron-phonon coupling [25]. In contrast, for nitrogen vacancy centers a Huang-Rhys factor of S = 3.73 [94] leads to nearly undetectable ZPL emission at room temperature and very strong sideband emission. Figure 1.6 displays an extremely simplified picture of electron-phonon coupling assuming that only one vibrational mode couples to the color center. Additionally, the nature of the mode responsible for the sideband transitions has not been discussed yet.

In a solid state host, different types of vibrational modes can lead to sideband emission: X Lattice modes: These modes correspond to lattice vibrations of the undisturbed diamond lattice. X Local and quasi-local modes: These modes are specific of the defect. They represent vibrations involving the defect and its neighboring carbon atoms. Coupling to lattice modes is governed by the phonon density of states of the diamond lattice. The density of states has been calculated and measured in the literature, e.g., in Refs. [25, 143–145]. Here, electronic transitions predominantly couple to phonons with wave vectors at the high symmetry points of the Brillouin zone, the so called critical points [25,139]. This has two reasons: First, these phonons have the shortest wavelengths. Thus, they can induce the strongest changes in interatomic distances, as their wavelengths are comparable to the spatial dimension of the color centers. This enables efficient coupling [25]. Second, the phonon density of states peaks at these points [25,139], as the phonon dispersion relations displays a vanishing slope [144,146]. A list of the phonon energies corresponding to these critical points is summarized in Ref. [147] and is displayed in Tab. 1.1. Electronic transitions predominantly couple to optical phonons as the anti-phase movement of the lattice atoms in these modes evidently induces strong interatomic distance changes. For acoustic modes, only short wave acoustic modes induce significant interatomic distance changes and thus couple efficiently. The phonon density of states in diamond has a sharp high energy cut off at around 165meV and diminishes strongly below approx. 70meV [25,143–145]. Therefore, all sideband features shifted less than 70 meV or more than 165 meV cannot be induced by modes of the diamond lattice: Features with high energy shift may arise from multi-phonon processes. However, for SiV centers, multi-phonon processes are very improbable and the features most probably arise from local modes of the color center. In contrast, the features with a low energy shift are fully attributed to local modes of the color center. Quasi-local and local modes arise solely due to the presence of the impurity. If the energy of these modes lies within the energy range of the lattice phonon density of states, the modes are referred to as quasi-local. If the energy is > 165meV or < 70 meV they are termed local modes. The vibrational frequencies of these modes are determined by the masses of the impurities as well as the interatomic bonding forces that act as springs for the vibration [25]. Brout and Vischer introduced a simplified model to determine the quasi-local mode frequencies  $\omega_{QL}$  and their resonance width  $\Delta\omega_{QL}$  for heavy impurities assuming that these impurities do not change the interatomic forces significantly [25,148].

$\omega_{QL} = \omega_{D} \sqrt{\frac{M_C + nM_I}{M_C}}$  (1.6)  $\Delta\omega_{QL} = \frac{\omega_D}{\sqrt{n}}$  (1.7) Here, MC and MI are the masses of the carbon atom and the impurity respectively. n denotes the number of impurity atoms participating in the vibration.  $\omega_D$  is the Debye frequency in diamond, which corresponds to 150 meV. For an impurity incorporating one Si atom, one would thus expect a quasi-local mode at 75 meV. Indeed, sidebands with a comparable energy shift at approx. 80meV have been observed (see Tab. 1.1). More advanced calculations using estimated force constants for lattice and defect were performed in Ref. [143]. The results for a Si atom sitting in a  $\text{Si}_2\text{C}$  site are summarized in Tab. 1.1, indicating the existence of several high energy local modes. Vibronic sidebands of SiV centers have been examined in several publications. The results are summarized in Tab. 1.1. Sittas et al. [115] examined the sideband structure in Si-doped HPHT diamonds. In low temperature experiments, they find a significant spectral narrowing of the three highest energy features corresponding to emission at 776 nm, 797 nm and 812 nm. Thus, they attribute these lines to purely electronic rather than vibronic transitions. This indicates that discrimination of vibronic sidebands and electronic transitions is not always clear as for defects involving heavy impurities the linewidths of sideband features due to local modes can be comparable to the

ZPL linewidth [25]. There are several indications in the literature that vibronic sidebands and, therefore, the linear electron-phonon coupling for SiV centers significantly depends on the local environment. Sternschulte et al. find a sideband feature shifted by 166meV only in some positions on a homoepitaxial CVD diamond [111]. Gorokhovsky et al. report that in polycrystalline diamond vibronic sideband features could not be resolved under non-resonant 514 nm laser excitation [112]. However, upon resonant excitation with 737 nm, a distinct sideband structure evolves. The authors explain that observation in terms of the excitation of only a sub-ensemble featuring a ZPL at the excitation laser wavelength. This sub-ensemble within the inhomogeneously broadened ensemble displays defined vibronic sidebands. These sidebands are spectrally washed-out if all inhomogeneously broadened SiV centers are excited and the differing sideband spectra add up. This observation supports the assumption of strongly environment dependent electron-phonon coupling. Thus consequently, for single emitters, one would also expect to observe varying vibronic sidebands for individual emitters. Additionally, the authors of Ref. [112] report that if the excitation wavelength is tuned to longer wavelengths, thus selecting another sub-ensemble, the vibronic sideband structure changes: The most prominent vibronic sideband now displays a smaller energy shift with respect to the ZPL. Thus, the energy of the corresponding phonon mode has to be reduced for the sub-ensemble selected with longer wavelength laser excitation. In contrast, the shifting behavior for a higher energy sideband shows no clear trend. Thus, different vibronic sidebands show a deviant behavior under environmental changes that shift the ZPL. Furthermore, simultaneously the width of the phonon sidebands changes [112]. As displayed in Tab. 1.1, vibronic sidebands identified as local modes as well as sidebands due to lattice phonons [147] have been reported for SiV centers. The reports in the literature display a spread in the observed positions and also in the number of features observed, again indicating a dependence on the environment. If the diamond lattice is stressed, lattice phonon energies change. Additionally, energetically degenerate phonon modes split up [149]. Shifting rates for the optical zone center phonon ( $165.2 \text{ meV} = 1332.4 \text{ cm}^{-1}$ ) amount to [149]  $\Delta E_{\text{hydro}} = 0.40 \pm 0.02 \text{ meV} \pm [111] = 0.27 \pm 0.02 \text{ meV} \pm [100] = 0.09 \pm 0.01 \text{ meV GPa GPa GPa}$  for hydrostatic pressure and compressive uniaxial stress along [111] or [100] direction. The optical zone center phonon is the only phonon were a direct observation of the shift due to stress is possible as it can be detected via Raman scattering of light. For local modes, however, no similar direct measurements of the phonon energies is possible. Thus, it is challenging to discriminate between changes in the electron-phonon coupling of a color center or changes in the mode frequencies.

## Chapter 3

# Photoluminescence Setup

The key measurements of this thesis are spectroscopic measurements of SiV centers in nanodiamonds. For this aim, a home-built confocal setup is used, which is described in this chapter.

The confocal setup serves to perform a series of spectroscopic measurements on fluorescence light: scanning the sample to find SiV centers, recording photoluminescence spectra of the aforementioned, determining the brightness of an emitter by recording the saturation count rate, and determine whether the emitter in question is a single emitter by performing photon autocorrelation ( $g^{(2)}$ ) measurements. The entire setup is built up by a confocal setup, to which a spectrometer or an Hanbury Brown and Twiss setup are attached:

- The confocal setup is the core component where the sample sits. The excitation laser light is focused on the sample by an objective and the fluorescence light from the SiV centers collected by the same objective, hence the name confocal. The sample can be moved to scan it in order to excite emitters and collect the fluorescence light. For scanning, an avalanche photo diode is attached to the confocal setup.
- The grating spectrometer to investigate the spectral properties of the emitters. This is crucial to distinguish between SiV centers, other color centers and nanodiamonds which do not host color centers.
- A Hanbury Brown and Twiss (HBT) setup to investigate the single photon character. It is built up of two avalanche photo diodes (APDs) which are also used for scanning the sample and for performing saturation measurements.

saturation  
already  
introduced?

### 3.1 Confocal Setup

Figure 3.1 depicts a sketch of the confocal setup. Except for the laser and the sample stage, the whole setup is fixed to a vertical breadboard. As this vertical design permits a horizontal sample stage, it allows for easy scanning and exchanging of the samples, without the need of gluing them to a vertical stage. The friction between the sample and the aluminum surface of the stage is sufficient that the sample does not get out of place during scanning. For some measurements it is important that the sample has a defined orientation. For this purpose it is possible to orient it with the help of an aluminum angle and adjust the orientation with a

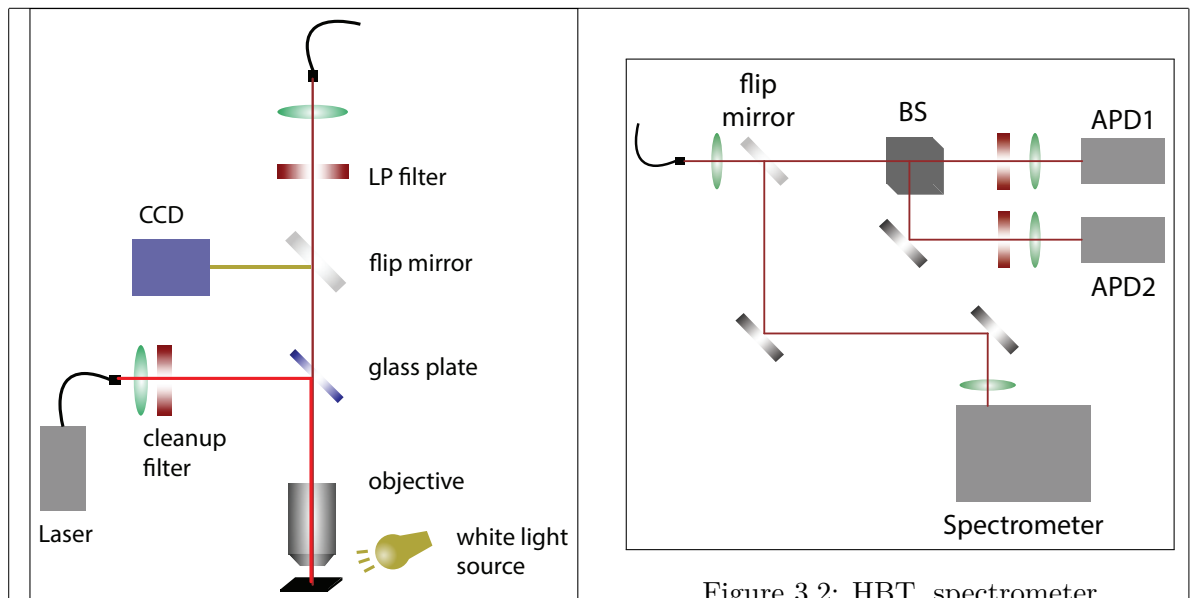


Figure 3.2: HBT, spectrometer

Figure 3.1: Confocal setup

manual rotation stage. In contrast, the translation stage is powered with two stepper motors (Newport MVP25XL) in the horizontal x and y directions. Above the horizontal stage, the objective is fixed to another stage which in turn is fixed to the vertical breadboard. In this way, the vertical z distance can be adjusted for focusing the laser light on the sample. It also enables scanning in the direction of the optical axis, which is coincides with the height of the sample. Therefore, three-axis scanning of the sample is implemented.

The bright red color in the sketch in Figure 3.1 represents the excitation beam path. The sample is excited with a continuous wave diode laser (Schäfter-Kirchhoff, 58FCM) which emits at a wavelength of 660 nm. The outlet of the laser is a pigtail fiber. The laser light is outcoupled and collimated exploiting an aspheric lens. To suppress sideband emission from the laser, a 660 nm bandpass filter with a filter window of 10 nm is used. After this cleanup filter, the excitation beam then hits a glass plate (fabricator Halle Germany) which guides the beam through a microscope objective to be focused on the sample. The microscope objective is of the type Olympus, LMPlanFLN 100x and has a numerical aperture of 0.8. As the luminescence light from the emitter is in the same focus as the excitation laser light, it is effectively collected by the objective (hence "confocal setup").

The collected light follows the detection beam path depicted in dark red in Figure 3.1. Both the excitation light reflected from the sample surface and the fluorescence light from the color centers pass through the glass plate. If the flip mirror behind the beamsplitter is taken out of the beam path, the beam is directed towards a single mode fiber which connects the confocal setup with either the spectrometer or the HBT setup. In front of the single mode fiber there is a longpass filter to filter out the residual excitation light and also ambient light. The filter is chosen with a cutoff wavelength of 710 nm or 720 nm. The fluorescence light is fed into the single-mode fiber (Thorlabs SM600) with an aspheric lens. Besides the obvious purpose of guiding the photoluminescence light to the spectrometer and the Hanbury Brown and Twiss setup for spectroscopic investigations, it has another crucial application: Its diameter of about 4.3  $\mu\text{m}$  serves as a pinhole to reject photoluminescence light from depths outside of the focal

thickness

plane [8]. For this axis the resolution amounts to , in the plane of the sample it is .

According to the experimental necessities, instead of the mentioned glass plate a dichroic mirror (DRLP692) can be employed. The dichroic mirror spectrally separates excitation light from photoluminescence light as it selectively transmits and reflects sight as a function of its wavelength. The glass plate features a high transmission of 90% and therefore exhibits a high collection efficiency of fluorescence light, but at the same time, 90% of the excitation light is lost, as it is not reflected towards the sample. In contrast to that the dichroic mirror allows for a higher excitation intensity using the same excitation laser which is necessary for instance for saturation measurements. However, a high excitation intensity may cause permanent fluorescence intermittence of the SiV centers (for further detail, refer to ). In general, if a high excitation is necessary, as for saturation measurements, the dichroic mirror is used; otherwise, the glass plate is used to collect as much fluorescence light as possible without damaging the SiV centers due to exposure to a high laser light intensity.

## 3.2 Optical Imaging of The Sample Surface

The confocal can be modified to investigate the sample surface before starting the fluorescence measurements. For this purpose, the sample is directly illuminated in a flat angle from outside the objective with white light from a halogen lamp (depicted as white light source in Figure 3.1). The flip mirror behind the glass plate is brought into an upright position to guide the light towards a CCD camera (). The scattered light from the sample surface is collected by the objective and the surface is imaged on the CCD chip . Hence Nanodiamonds and other features on the substrate are visible. The resolution of this configuration of the setup is limited by .

In chapter ?? an application of the nanodiamond is introduced, for which it is of major importance to know the position of specific nanodiamonds. Therefore, cross markers are milled into the surface of the substrate on which the nanodiamonds are situated. These markers of a size of 10  $\mu\text{m}$  can easily be recognized by optical iamging. The starting point for a scan of an area of interest on the sample is fixed while navigating with the optical image. After flipping the flip mirror, a photoluminescence scan of that area is started.

## 3.3 Spectrometer

Figure 3.2 displays the detection part of the setup. The fluorescence light from the fiber which connects the confocal setup with the detection setup is outcoupled with an aspheric lens. A flip mirror is employed to direct the light either to a grating spectrometer or the HBT setup. The optical spectrum of a light source gives insight to the optically active constituents and therefore bears information about the emitter.

As mentioned before, the fluorescence light from the SiV centers is investigated with the grating spectrometer (Princeton Instruments Acton2500i). The incident beam passes through an entrance slit, is then scattered on the grating where the light is spectrally divided and finally hits a detector, imaging the entrance slit on the detector surface. The employed detector is a CCD camera ()which is cooled with liquid nitrogen to a temperature of  $-120^\circ\text{C}$  for background reduction due to thermally generated free charge carriers. It is optimized for

value

value

short discussion  
if resolution is enoughcheck  
numberinsert  
chapter

specs

resolution  
CCDoptical  
diffrac-  
tion,  
shadows

type

detection of light up to a wavelength of 900 nm. The spectrometer features three gratings: 600 grooves/mm, 1200 grooves/mm, and 1800 grooves/mm. These gratings are mounted on a turret, allowing easy switching of the gratings between measurements.

With the spectrometer's step-and-glue function which is implemented in the spectrometer software (WinSpec) it is possible, to record several spectra over a wide wavelength range which are then stitched together. It is therefore possible to combine a larger wavelength range with a higher resolution. For most measurements the grating with 600 grooves/mm was used. The resolution of the spectrometer using the 600 grooves mm<sup>-1</sup> is 0.13 nm at 738 nm and the accuracy amounts to  $\pm 0.4$  as stated by the manufacturer. This resolution suffices for most of the measurements mentioned in this work.

### 3.4 Hanbury Brown and Twiss Setup

A Hanbury Brown and Twiss setup serves to record the photon autocorrelation function ( $g^{(2)}$  function) of an emitter. In this work, the  $g^{(2)}$  function is used to make statements about whether a photoluminescence source emits single photons and is therefore one single emitter. In the photon number representation, it is defined as follows:

$$g^{(2)}(0) = \frac{\langle N(t)N(t + \tau) \rangle}{\langle N(t) \rangle^2}.$$

Here,  $N(t)$  denotes the photon at a certain time  $t$ ,  $N(t + \tau)$  denotes the photon at a time interval  $\tau$  later than  $t$ . The angular brackets  $\langle \rangle$  denote the temporal averaging. The physical explanation is that if the source is a single emitter and emits a photon at a time  $t$ , the next time any photon is recorded is at time  $t + \tau$ . For a time interval close to zero, the value of the  $g^{(2)}$  function must ideally approach zero or at least be smaller than 0.5 if only a single emitter is present: The denominator is zero, because  $N(t + \tau)(\tau = 0) = 0$  due to only one photon, namely  $N(t)$  being present. If two photons are emitted at the same time (time delay zero), the  $g^{(2)}$  function yields  $g^{(2)}(0) = 0.5$ . (For a detailed explanation of the  $g^{(2)}$  function read [9])

The principle of the HBT setup is to evaluate the time delay between two consecutive photons. A sketch of the HBT setup is shown in Figure 3.2. The photons are detected with single photon avalanche photo diodes (APDs) of the type PicoQuant τ-SPAD100. APDs are the semiconductor analog to photomultiplier tubes: An incoming photon creates secondary charge carriers through ionization. The secondary charge carrier is accelerated by a bias voltage to create more secondary charge carriers, resulting in an avalanche effect. Therefore, the signal of a single photon is intensified and detected as an electrical current pulse. These avalanche photo diodes have a nominal detection efficiency of up to 70% at an optimal wavelength of about 670 nm and a dark count rate of under 100 cps. If a charge carrier created by the avalanche is trapped and later liberated, it induces a so-called afterpulse. To avoid detecting these artifacts as real events, the APDs have a dead time of about 70 ns. In the ideal case, one APD would be enough to measure the time delay between two consecutive photons. However, the second of two consecutive photons could hit the detector during its dead time. To circumvent this problem, two APDs are employed and the detection beam is split with a non-polarizing 50:50 beamsplitter cube. Each beam then passes through a bandpass filter and is focused on the avalanche photo diode with an aspheric lens. As the beam path is slightly different for each APD, a small optical path difference is introduced, however, this difference

fox nach  
lesen

only results in an offset of the  $g^{(2)}$  function and does not alter the physical nature of the result. The bandpass filters serve two purposes: First, they limit optical crosstalk between the avalanche photo diodes. The detection process in an avalanche photo diode produces light due to recombination of charge carriers. Crosstalk between two avalanche photo diodes occurs, if one of the photons produced by recombination in one avalanche photo diode escapes and is detected in the other one [10]. Secondly, the bandpass filters serve to reduce background during the  $g^{(2)}$  measurement process or to spectrally divide emission from several emitters. Therefore, it is possible to find single emitters, which are not spatially separated enough to be separated by the spatial resolution of the setup: They can be individually investigated if their ZPLs exhibit wavelengths which are spectrally well separated. Bandpass filters suited for the respective wavelengths are used to investigate light from one of the ZPLs.

When the APD fires, it outputs a digital TTL (transistor-transistor logic compatible) signal. The arrival times of the signals (so-called time tags) are recorded with a time tag unit (produced by dotfast-consulting, timing resolution 78.125 ps). The timing uncertainty of the photon detection process introduces variations of the digital signal's time tag from the actual detection time. Note that this error does not represent the time evolving from the photon impact to recording, but solely the uncertainty of the exact recording time. This process is called timing jitter. It affects the time tags and with them the physical nature of the  $g^{(2)}$  function. A discussion of the impact of timing jitter will be given in ??.

As stated earlier, the time delay between two consecutive photons is necessary for the reconstruction of the  $g^{(2)}$  function. The time delays are fed into a histogram which is then fitted to receive the continuous  $g^{(2)}$  function. In the Hanbury Brown and Twiss-setup the arrival time of the photons are measured with two APDs and for each APD one list of arrival times is recorded as raw data. To get a single array of arrival times of the photons, which can then be binned to obtain the  $g^{(2)}$  function, the arrays of time tags of the two APDs have to be correlated. For that, the time difference between each entry in one array and all consecutive time tags in the other array are determined and stored according a binning defined by the timing resolution of the time tag unit. After normalizing and fitting these data, statements about whether the emitter is a single emitter can be made.

wording

put in reference

---

---

## Chapter 4

# Fabrication of Nanodiamonds

“Diamond forms under high temperature and pressure conditions that exist only about 100 miles beneath the earth’s surface.” (Homepage of the Gemological Institute of America Inc.) While this statement is true for natural gem diamonds, various methods exist to synthetically produce diamond for applications in industry and research. In this chapter, different fabrication methods of diamonds and nanodiamonds in particular are explained. The first two procedures described are the high-pressure, high-temperature method and the chemical vapor deposition are described. These are two of the most commonly used fabrication methods for laboratory-produced diamonds. The high-pressure, high-temperature (HPHT) process mimics natural conditions under which diamond is formed within earth and is widely used to synthetically produce diamonds for industry. While these HPHT diamonds are exploited for some experiments reported in this work, most measurements which are subject in this thesis are carried out on diamond produced with a CVD process. The third method which is described is the wet-milling process in a vibrational mill, which is a technique using chemical vapor deposition or HPHT diamond. Nanodiamonds produced with this milling process are the main focus of this thesis. It has to be stressed, that in contrast to the first two methods described in this chapter, the wet-milling process is not a process to produce diamond itself, rather it serves to crush bigger diamond starting material into pieces of a desired size. For a more extensive list of diamond production processes refer to e.g. [11]. Aside from the general diamond fabrication processes, the production details of the nanodiamonds used for this thesis will be mentioned.

### 4.1 High-Pressure High-Temperature Diamond

The HPHT process was the first process to successfully synthesize diamond (in 1879). Temperatures of a few thousand degrees Celsius and pressures between 50 000 bar and 100 000 bar are needed [11]. Today, it is still widely used due to its relatively cheap production costs [12]. In the HPHT process, diamond is synthesized from graphite. The machine used for this kind of synthesis is a press. For some forms of this method, a metallic solvent is added which lowers the needed pressures; the solvent causes the graphite to dissolve at lower pressures and temperatures, and at the same time it causes the diamond to crystallize. Several press designs exist, which all provide a high temperature and a high pressure in their core. While it is possible to grow big ( $> 10$  carat) high-quality diamonds with the HPHT process, it is

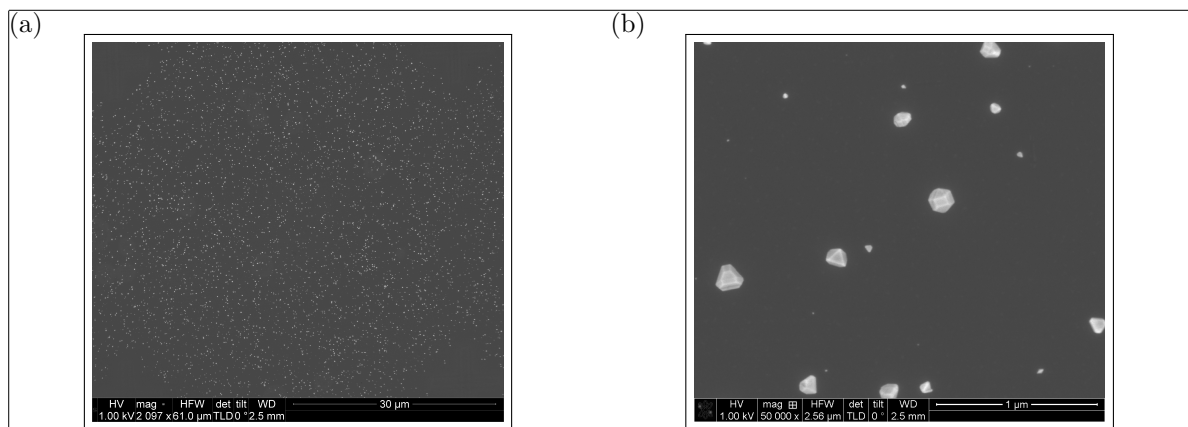


Figure 4.1: SEM images of CVD grown diamonds (sample insitucvd) produced by M. Schreck's group (Augsburg University). The average size of these nanodiamonds is 100 nm. (a) Overview image, white dots are nanodiamonds. (b) Detail image, it can be seen that not all nanodiamonds exhibit the same size and that they coexist in different shapes.

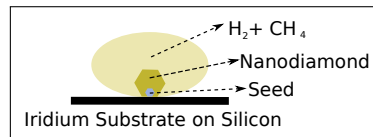


Figure 4.2: Sketch showing the production of CVD nanodiamonds in the growth chamber with a methane gas environment.

rather expensive when compared to the CVD process due to the necessary high temperatures and high pressures.

In the scope of this thesis, HPHT diamonds produced by Davydov et al. [13] are spectroscopically investigated.

## 4.2 Chemical Vapor Deposition Diamond

In contrast to the HPHT process, during the chemical vapor deposition process, diamond is grown from a vapor phase. This process requires moderate temperatures ( $700^{\circ}\text{C}$  to  $1300^{\circ}\text{C}$ ) but low pressures of less than 1 bar in a vacuum chamber [] The diamond in a metastable state Atomic hydrogen is necessary to suppress the simultaneous growth of graphite. The vapor phase within the growth chamber is a mixture of hydrogen and methane, the latter of which acts as a carbon source. Within the vacuum chamber, activation of the gas by an energy source (e.g. microwave plasma) breaks apart the gas molecules to release carbon atoms. These atoms are drawn down toward the cooler substrate. On the substrate surface, various processes occur, such as adsorption, desorption and diffusion. The growth parameters are optimized such that growth of diamond is favored with respect to graphite.

Growth on a substrate is easier, if the lattice constant of the substrate and the crystal to be grown are very similar. The lattice constant of iridium ( $0.384\text{ nm}$ [14, 15]) is very similar to the lattice constant of diamond ( $0.356\text{ nm}$ [16]). Therefore, the diamonds were grown on a stratified substrate, consisting of iridium layers of  $60\text{ nm}$  to  $150\text{ nm}$  thickness grown onto an

sind die  
nicht  
auch zer-  
mahlen  
worden?

wie kom-  
men da  
die SiVs  
rein?

ueberleitu-  
zu naech-  
stem  
satz

yttria-stabilized zirconia (YSZ) buffer layer, which in turn was grown on a silicon wafer [17]. If the lattice constant of the substrate and the diamond are not matched, stress in the diamond lattice is induced. Therefore, the iridium substrate not only facilitates diamond growth, but also reduces unfavorable stress in the nanodiamonds (more on the effect of stress in ??).

For crystals to form in heteroepitactic growth (i.e. one type of crystal is grown upon the surface of a different type), a nucleation step is necessary [18]. The easiest method to obtain nuclei on a substrate is to spin-coat the substrate with small diamond seed crystals of a size of a few nanometers. This method is exploited for all the CVD grown nanodiamonds investigated in this thesis. Such small seed diamond crystals are commercially available, and are usually diamond particles produced by a so-called detonation process. In a detonation process, the high pressure produced by shockwaves of a detonation is used to create very small diamond particles of a size down to a few nanometers. During the CVD growth process, carbon from the methane gas is adsorbed to the seed crystals. To produce nanodiamonds of a desired size, the growth process is stopped when the diamonds grown onto the seed crystals reaches the desired size. If the growth process is continued, the individual crystals grow together to form diamond films. Such diamond films are used as starting material for the wet-milling process described in the next section (section 4.3)

One of the advantages of the CVD process is that silicon is incorporated *in-situ*. This is achieved by etching of silicon substrate edges by the plasma which automatically occurs in the growth chamber and silicon atoms diffuse into the methane gas. For a higher silicon content in the diamond, sacrificial silicon is put into the growth chamber. These atoms are then built into the diamond lattice while growth.

After nanodiamond growth, the nanodiamonds are either investigated directly on the growth substrate or they are shaken off in an ultrasonic bath to obtain a solution which is coated onto other substrates for further measurements.

In this thesis, two types of samples were investigated which were directly produced as nanodiamonds.<sup>1</sup> The first batch (henceforth called CVD samples) were grown on detonation diamond seeds of a size smaller than 3 nm (produced by the company Microdiamant, product Liquid Diamond monocrystalline, MSY 0-0.03 micron GAF). For the growth process, 1% of methane is added to the hydrogen environment in the growth chamber. The growth process is performed with a pressure of 30 hPa for 30 min to 60 min, yielding nanodiamonds of a diameter of about 100 nm to 200 nm.

The other samples directly produced by a CVD process are nanodiamonds grown onto molecular analogs of diamond crystals. A subgroup of these molecular diamonds are called diamondoids and are carbon crystals based on the carbon cage molecule adamantine  $C_{10}H_{16}$ . The molecular diamonds used for this work are adamantine in cyclohexane, mercapto adamantine in cyclohexane, and cyclohexane. Each of these seed crystals is used in different growth processes. During the growth process, either 3% or 1% methane was added to the hydrogen plasma and either silicon or silicon dioxide was exploited to form *in-situ* incorporated SiV centers (see Table 4.1).

is this  
correct?

irgendwo  
einfue-  
gen, was  
ich dies-  
bezgl.  
gemacht  
hab

put in  
figure

### 4.3 Wet-Milled Nanodiamonds

Apart from growing nanodiamonds of a specific size directly via a CVD process, macroscopic diamond starting material can be crushed to obtain small diamond particles. In contrast

<sup>1</sup>The CVD nanodiamonds were grown by the group of M. Schreck, Augsburg University[].

Table 4.1: Summary of the samples grown on diamondoid seed crystals.

Sample name	Seed crystals	Methane conc.	Silicon source
160211_E	Mercapto adamentane in cyclohexane	1%	SiO <sub>2</sub>
160211_F	Cyclohexane	1%	SiO <sub>2</sub>
160212_C	Cyclohexane	3%	silicon
160212_D	Adamentane in cyclohexane	3%	SiO <sub>2</sub>
160212_E	Mercapto adamentane in cyclohexane	3%	SiOs
160212_F	Cyclohexane	3%	SiO <sub>2</sub>

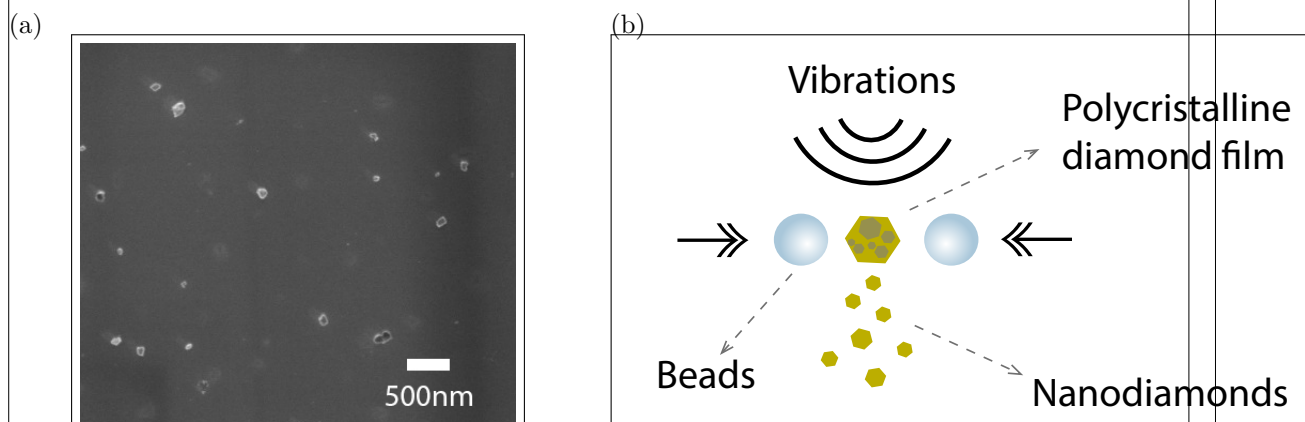


Figure 4.3: Pictures of the milled nanodiamonds (sample insitu100). (a) SEM picture showing the distribution of the nanodiamond crystals on the iridium substrate (sample insitu100). (b) Sketch showing the wet-milling process in a vibrational mill. Vibrations from the mill drive the beads which collide with the diamond material and crush it to smaller pieces.

to nanodiamonds directly grown by a CVD process, the process is divided into two subprocesses: 1. Diamond is produced, for example by an HPHT process or by CVD growth. 2. The macroscopic diamond is milled to smaller diamond particles. For the wet-milling process which yields the nanodiamonds investigated in this thesis<sup>2</sup>, small beads are used to crush the diamond material. The beads are driven by vibrations of a vibrational mill. A sketch of the process is shown in ??.

The big advantage of the milling process is that it enables the production of a large quantity of diamond nanoparticles. When producing nanodiamonds directly via a CVD process, the number of produced nanodiamonds in one process scales with the surface of the substrate on which the nanodiamonds are grown. In contrast, the quantity of milled nanodiamonds scales with the volume of the starting material. Therefore in one and the same process the limit for the obtainable amount of diamond nanoparticles is much higher. Another advantage of the milling process is that the nanodiamonds are in an aqueous solution after milling. Therefore, it is viable to spin-coat the nanodiamonds directly onto any substrate suited for further experiments without further treatment.

The wet-milled nanodiamonds have the disadvantage to contain grain boundaries, resulting in reduced crystal quality (described in more detail in 5.3). While the polycrystalline diamond film is more likely to break apart at grain boundaries, the final nanodiamonds still contain grain boundaries. In contrast, as-grown CVD nanodiamonds are mainly single crystals.

After milling, the nanodiamonds are treated with post-processing steps including annealing in vacuum and oxidation in air. A detailed description of the processes and their impact is given in 5.

In principle diamond produced by any production method can be used as starting material for the milling process. In the following sections, they are distinguished by the respective starting material and milling method.

### 4.3.1 Wet-Milled HPHT Nanodiamonds

We investigated nanodiamonds, which were produced from a HPHT starting material and milled by a wet-milling process to median sizes of about 45 nm, 80 nm and 260 nm. They were then drop-casted onto an iridium substrate and implanted with  $^{28}\text{Si}^{1+}$ <sup>3</sup>. At last, all HPHT nanodiamonds (samples hphtimp45, hphtimp80, hphtimp260) were oxidized in air at  $450^\circ\text{C}$  for 3 h.

### 4.3.2 Wet-Milled chemical vapor deposition Nanodiamonds

In the following paragraphs, details of the production processes of nanodiamond produced by wet-milling a CVD diamond film in a vibrational mill are described. For an overview of the samples refer to Table 4.2. The starting material for the wet-milled nanodiamonds was a nanocrystalline diamond film [19] directly grown on a silicon wafer by CVD. A microwave hydrogen plasma containing 1% methane was used to grow on purified 5 nm nanodiamond seeds

<sup>2</sup>If not otherwise stated, all the mentioned wet-milling processes were carried out by Andreas Muzha in the group of A. Krueger (Julius-Maximilians Universität Würzburg))

<sup>3</sup>Implantation was performed by D. Rogalla, Ruhr-Universität Bochum (RUBION - Zentrale Einrichtung für Ionenstrahlen und Radionuklide)

info  
about vi-  
brational  
mill

more info

besser  
for-  
mulieren

etwas an-  
ders fo-  
mulieren

implantati-  
on pa-  
ramete-  
rs

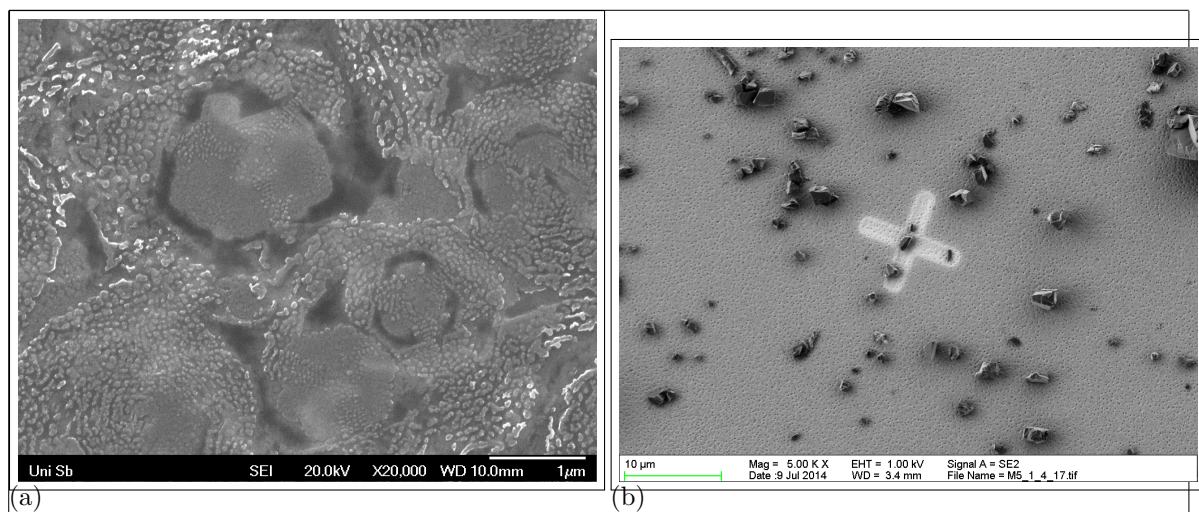


Figure 4.4: (a) SEM picture of nanodiamonds sunken into a silicon substrate after annealing at 900 °C for 3 h. Magnification 20 000. (b) SEM image of the microdiamonds after milling on an iridium substrate, but before implantation. In the middle of the picture, there is a reference cross milled into the iridium substrate with a focused ion beam. Its size amounts to 10  $\mu\text{m}$ . It can be seen, that the microdiamonds exhibit sizes of a few micrometer.

(produced by PlasmaChem). To induce *in-situ* SiV center creation, sacrificial Silicon pieces are situated in the growth chamber. During diamond growth the silicon pieces are etched by the plasma and individual atoms are incorporated into the diamond lattice. The diamond film is then milled by a wet-milling process in a vibrational mill with steel beads. The high amount of steel containment due to the steel beads is removed by extensive acid treatment. We also investigated nanodiamonds milled with silicon nitride beads, and found that the choice of material of the beads does not cause any spectroscopic difference ???. The median diameters of the diamonds are 50 nm, 70 nm and 100 nm (Figure 4.3a). The particle sizes are determined with laser diffraction spectroscopy. Transmission Electron Microscopy (TEM) pictures of the diamond crystals show that the milled nanodiamonds are polycrystalline, exhibiting a typical size of single crystals of a few tens of nanometers. In ?? a TEM image of a typical nanodiamond is shown. Crystal boundaries have effects on the formation of color centers: SiV centers are more prone to form at crystal boundaries [20]. The aqueous solution containing the nanodiamonds is drop cast onto an iridium film on a Silicon substrate. The iridium film of a thickness of 130 nm is grown onto a buffer layer of yttria-stabilized zirconia (YSZ) which in turn is grown onto a Silicon wafer. The iridium surface has the advantage that it acts as an antenna and therefore enhances the collection efficiency of fluorescence light [21] (for more information on the substrate see section 4.4). Post-process treatment comprises either both annealing in vacuum at 900 °C and consecutive oxidation in air at a temperature of 450 °C, or only one of the two methods. The duration for either treatment method was 3-6 hours.

### 4.3.3 Doubly Wet-Milled Implanted Nanodiamonds Implanted With Silicon

We also investigated nanodiamonds with SiV centers implanted after diamond growth. Starting material was a polycrystalline Element Six diamond film (electronic grade). In bulk material, the implantation causes the SiV centers to form in a specific depth dependent on the implantation energy, leaving most of the diamond vacant of SiV centers. As a consequence, a big portion of nanodiamonds milled from such a bulk material would not host any SiV centers. To obtain diamond particles with a homogeneous distribution of SiV centers, the process of fabricating implanted nanodiamonds is the following. First, the diamond film is milled to diamond particles of sizes of a few micrometers. In the second step, these microdiamonds are then spin-coated onto iridium substrates and implanted with  $^{28}\text{Si}^{1+}$ . To eliminate lattice damage and vacancies formed by the implantation process, the diamonds were annealed in vacuum and subsequently oxidized. At last, the micrometer sized diamond particles are milled to smaller sizes.

#### Preliminary Tests

The starting material was an Element Six electronic grade diamond film. The diamond was milled in a wet-milling process to sizes on the order of micrometers, which were then coated onto a silicon substrate. The microdiamonds were implanted with  $^{28}\text{Si}^{1+}$  at an implantation energy of 1.7 MeV, and fluences of  $10^9 \text{ cm}^{-2}$  to  $10^{12} \text{ cm}^{-2}$ <sup>4</sup>. After implantation, the microdiamonds on the silicon substrate were annealed for 2 h at 900 °C and oxidized in air for another 2 h at 450 °C. However, we encountered the problem that the silicon sublimated and re-nucleated during annealing, causing the diamonds to sink into the silicon surface (Figure 4.4a). Iridium is less prone to damage by high temperatures and withstands annealing procedures up to our standard annealing temperature of 900 °C without problems. Therefore, we used a sample with microdiamonds on a silicon substrate which was not annealed to shake the nanodiamonds off the silicon substrate in an ultrasonic bath, and consecutively coated the microdiamonds on an iridium substrate. After annealing and oxidizing the nanodiamonds on the iridium substrate, the iridium surface was intact.

#### Final Procedure

For the milling process in a vibrational mill, a minimum amount of diamond material is necessary. When starting with a diamond film, this threshold is easily reached, however, a big quantity of microdiamonds is needed to meet the requirements. Therefore, production was carried out at a larger scale after the preliminary tests. The microdiamonds were directly spin-coated onto iridium substrates, implanted with  $^{28}\text{Si}^{1+}$  (implantation energy 900 keV, fluence  $10^{11} \text{ cm}^{-2}$ )<sup>5</sup>. The microdiamonds were then annealed in vacuum for 3 h at 900 °C and oxidized in air for 3 h at 450 °C. At last, they were milled again to sizes of about 40 nm, 45 nm, 240 nm and 260 nm. The diamonds of sizes 40 nm and 240 nm were annealed in vacuum at 1200 °C.

how  
much?

time?

<sup>4</sup>Implantation performed by D. Rogalla, Ruhr-Universität Bochum (RUBION - Zentrale Einrichtung für Ionenstrahlen und Radionuklide).

<sup>5</sup>Implantation performed by J. Klug at rubitec - Gesellschaft für Innovation und Technologie der Ruhr-Universität Bochum mbH.

Table 4.2: Summary of the wet-milled samples. The first column indicates the names of the samples, the second the mean diameter of the nanodiamonds, and the third describes how the silicon was incorporated into the diamond.

Sample name	Size	Si incorporation	Post-processing
hphtimp45	45 nm	<i>implanted</i>	oxidized in air at 450 °C
hphtimp80	80 nm	<i>in-situ</i>	annealed in vacuum for 1 h at 1000 °C and at 900 °C for 3 h
hphtimp260	260 nm	<i>in-situ</i>	oxidized in air at 450 °C
insitu50	50 nm	<i>in-situ</i>	series of individual samples with diverse post-processing steps
insitu70	70 nm	<i>in-situ</i>	series of individual samples with diverse post-processing steps
insitu70n	70 nm	<i>in-situ</i>	no post-processing subset of insitu70
insitu70o	70 nm	<i>in-situ</i>	oxidized in air at 450 °C subset of insitu70
insitu100	100 nm	<i>in-situ</i>	series of individual samples with diverse post-processing steps
insitu100ao	100 nm	<i>in-situ</i>	annealed in vacuum at 900 °C, consecutively oxidized in air at 450 °C subset of insitu100
implanted250ao	250 nm	implanted	annealed in vacuum at 900 °C, consecutively oxidized in air at 450 °C
hphtimp260	40 nm	implanted	annealed in vacuum at 1200 °C, consecutively oxidized in air at 450 °C
hphtimp260	50 nm	implanted	oxidized in air at 450 °C
hphtimp260	240 nm	implanted	annealed in vacuum at 1200 °C, consecutively oxidized in air at 450 °C
hphtimp260	260 nm	implanted	oxidized in air at 450 °C

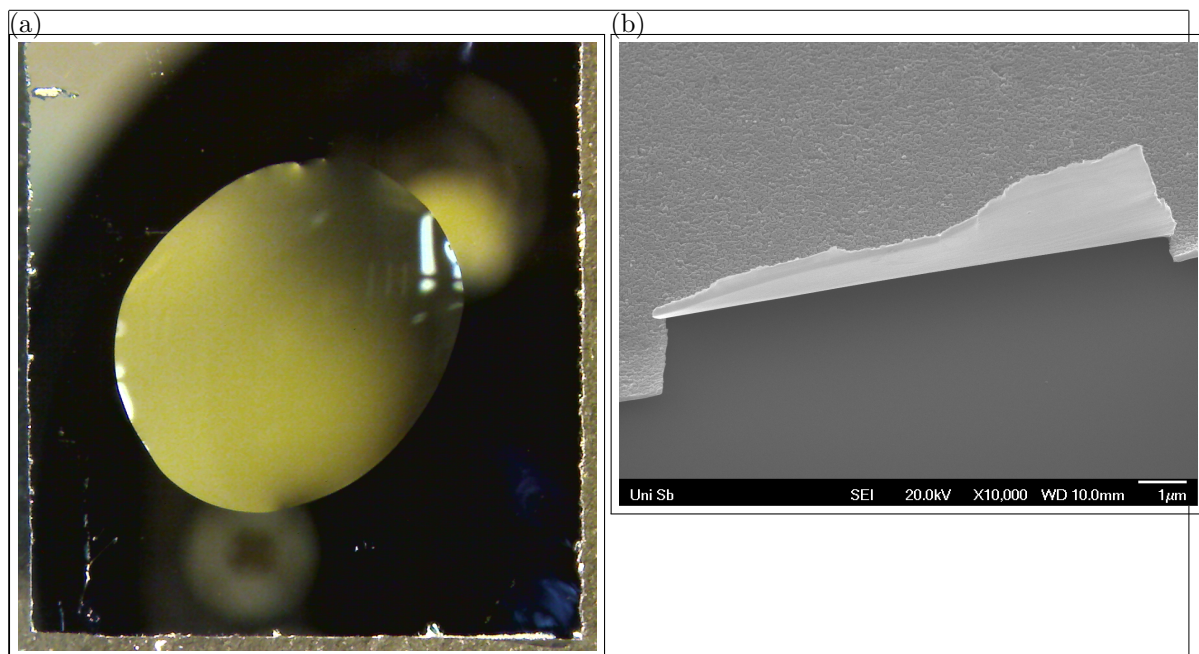


Figure 4.5: (a) Microscope image of a drop of water on an iridium substrate cleaned with Piranha etch. This picture was used to estimate the contact angle. (b) SEM picture of an 60 nm iridium layer that peeled off the substrate after an ultrasonic bath.

## 4.4 Iridium Substrate

As mentioned in section 4.2, we used a silicon substrate with an iridium layer on top for most experiments in order to match the lattice constant of diamond. We also use the same substrates for the experiments with wet-milled diamonds, as the iridium exhibits further advantages:

- The high hydrophilicity of iridium enhances the homogeneity of the nanodiamonds on the substrate after spin-coating or drop-casting. The hydrophilicity is further improved by treating the substrate in a Piranha etch (50:50 mixture of sulfuric acid  $H_2SO_4$  and hydrogen peroxide  $H_2O_2$ ) by removing oxide layers on the surface. The treatment with Piranha etch also has the advantage that all organic contamination is removed. Measurements after applying the Piranha cleaning yielded an estimation of the contact angle of slightly more than one degree. To determine the contact angle with water, the volume of a water drop is compared to the surface it covers after dropping it onto an iridium substrate. From that an estimation of the contact angle is deduced.
- During the post-processing steps, it is of major importance, that the substrate can withstand high temperatures. As described in section 4.3.3 during the preliminary tests with implanted nanodiamonds on a silicon substrate (sample name  , we encountered difficulties with diamonds on a silicon substrate as the sunk into the surface after annealing. In contrast, iridium withstands the used annealing process without damage.
- Additionally to the mentioned technical advantages, another advantage of the iridium surface manifests itself during spectroscopic measurements: Iridium acts both as a mirror and as an antenna for the fluorescence light emitted by the SiV center [21].

check  
numbers

sample  
name

Therefore, the collection efficiency of the fluorescence light is enhanced.

These advantages of iridium surfaces are only countered by one minor disadvantage: If the iridium layer is too thin, it tends to peel off the substrate (Figure 4.5b). We encountered this problem during a cleaning procedure in the ultrasonic bath. However, this disadvantage is easily circumvented by using a thicker iridium layer. For our measurements, we used an iridium layer of a thickness of 130 nm, with which we did not encounter any adhesion problems.

#### 4.4.1 Preparation of The Substrate

Prior to drop casting, the substrate is cleaned. The standard cleaning procedure comprised the following cleaning steps in an ultrasonic bath (3 min to 7 min each):

- Distilled water with a drop of dishwasher detergent
- Isopropanol (99.9% p.a.)
- Acetone (99.9% p.a.)
- Distilled water

Thereafter, the substrates are put into a Piranha solution (50% sulfuric acid  $H_2SO_4$ , 50% hydrogen peroxide  $H_2O_2$ ) to enhance the surface hydrophilicity and therefore obtain a homogeneous distribution of diamonds on the surface. They are then put again into distilled water and blown dry with compressed air to avoid residue from the water. The substrates were then either drop-casted or spin-coated with aqueous diamond solutions. For the prior, the substrates are heated to a temperature of 60 °C and drops of a volume of about 5  $\mu L$  dropped onto the substrate. If substantially more than 5  $\mu L$  is needed, the several drops of about 5  $\mu L$  are dropped onto the substrate consecutively, as with a single big drop the solution would flow off the substrate before drying. For spin-coating, a home built spin coater was used. Drops of 5  $\mu L$  are dropped on the substrate and the spin-coater set to a velocity of 2500 rpm for 3 min.

## Chapter 5

# Crystal Quality of Nanodiamonds

Crystal quality is the a measure for how close a crystal resembles its pristine form[]. Vacancies, impurity atoms and inclusions of graphite or amorphous carbon are examples for factors which decrease the crystal quality ???. Poor crystal quality manifests itself in photoluminescence spectra e.g. as broad spectral background fluorescence. To improve crystal quality, two methods are used: annealing in vacuum and oxidation in air. We investigated the effect of oxidation on the Raman spectrum. Raman spectroscopy of various samples gives insight to crystal quality and surface contamination. Raman scattering is the inelastic scattering of a photon  $\hbar\omega_i$  on a molecule or crystal lattice in the initial state  $|i\rangle$  with energy  $E_i$ . The molecule of cristal transitions into a higher energy state  $E_f$  and the scattered photon with frequency  $\omega_s$  looses the energy  $\Delta E = E_f - E_i = \hbar(\omega_i - \omega_s)$ . Therefore, energy from is exchanged between the photon and the excited matter, changing the rotational or oscillation energy of the involved molecule or the oscillation energy, i.e. phonons of the crystal lattice. The Raman shift is typically referenced in wavenumbers. It is calculated by:

$$\Delta\omega = \left( \frac{1}{\lambda_{ex}} - \frac{1}{\lambda_R} \right) \quad (5.1)$$

As every solid exhibits characteristic phonon modes, Raman spectroscopy is used to identify the contributing elements of a solid, hence in our case determine the purity of the diamond and identify contamination with  $sp^2$  bonded and amorphous carbon, and graphite. Also, the Raman spectrum changes under the influence of stress in the sample, providing a way to investigate the stress in the sample with opical means. Additionally, several transmission electron microscopy (TEM) measurements exhibit the composition of the wet-milled nanodiamonds. During transmission electron microscopy a beam of electrons is transmitted through a sample, forming an image of the transmitted sample. Due to the smaller de Broglie wavelengths of electrons as compared to photons, a higher resolution is obtainable, and the crystal lattice planes can be resolved. Therefore, the crystal quality can be investigated from a morphological point of view.

ist das  
Wort  
richtig?

maybe  
rephrase

## 5.1 Post-Processing Treatments

### 5.1.1 Annealing and Oxidation

During silicon implantation the diamond lattice gets damaged by the penetrating ions.  $sp^2$  bonds, carbon interstitials and vacancies disrupt the metastable equilibrium of the diamond phase. Hence, there is a tendency for damaged diamond to "tip over" to the thermodynamically stable form of carbon, i.e. graphite. At temperatures above about  $500^\circ\text{C}$ , vacancies in the diamond lattice become mobile and diffuse towards the surface[22]. Literature suggests, that annealing at  $900^\circ\text{C}$  for 1 h is sufficient to remove most of the damage following implantations, that however some damage remains even after annealing at  $900^\circ\text{C}$  for 1 h. To reduce the damage in the diamond lattice, we anneal the implanted diamonds at  $900^\circ\text{C}$  to  $1200^\circ\text{C}$  for 3 h to 6 h in vacuum ( $10^{-6}\text{ Pa}$ ).

The surface of the nanodiamonds is contaminated with graphite and amorphous  $sp^2$  hybridized carbon . The vacancies which diffuse towards the surface during annealing further increase the amorphous carbon content on the surface of the nanodiamonds []. We apply oxidation in an oven under ambient air at a temperature of  $450^\circ\text{C}$  for 3 h to 6 h.

another citation

warum

### 5.1.2 Surface Treatment With Gas And Plasma

We wanted to know whether surface treatment with different gasses had an influence on the emission properties, so we treated them with hydrogen ( $\text{H}_2$ ), oxygen ( $\text{O}_2$ ), ozone ( $\text{O}_3$ ) all both at room temperature and at  $500^\circ\text{C}$ ; and also with  $\text{H}_2$  plasma. However, we found that most nanodiamonds treated in this way only showed luminescence which immediately bleached when illuminated with a cw  $660\text{ nm}$  laser even at low excitation powers of  $200\text{ }\mu\text{W}$ , or no luminescence at all. We double-checked with a CCD-image of the surface to be sure that there are nanodiamonds in the focus. This bleaching occurred so quickly, that after a scanning no spectrum could be taken. The only samples which did yield spectra with measureable ZPLs were the ones treated with  $\text{H}_2$ . However, also these SiV centers were not single ones. Therefore, we did not further investigate these samples.

One sample showed shells around the nanodiamond after oxidizing in air. We attribute this effect to a contamination in the oven. When we illuminated these nanodiamonds in the SEM for several moments, the shell went away. We therefore deducted that the shell is organic material. To get rid of the shells on the whole sample, we treated it with oxygen-argon plasma for 3 min<sup>1</sup>. After the first treatment, the shells were smaller, but not gone. So we put them into the oxygen-argon plasma again for 3 min, however, the shells were bigger than before any treatment. We tried another approach to get rid of the shells with ozon treatment for 4 h at  $360^\circ\text{C}$ . Before ozon treatment there the diamond Raman line and other Raman lines visible. After surface treatment, more lines appeared and all of these other lines got more intense. There are probably organic contaminations on the sample in which functional groups got introduced by the ozon treatment. We did not further investigate this sample and defined it as broken.

beginning new text

end new text

<sup>1</sup>Treatment performed by J. Schmauch, group of R. Birringer, Saarland University

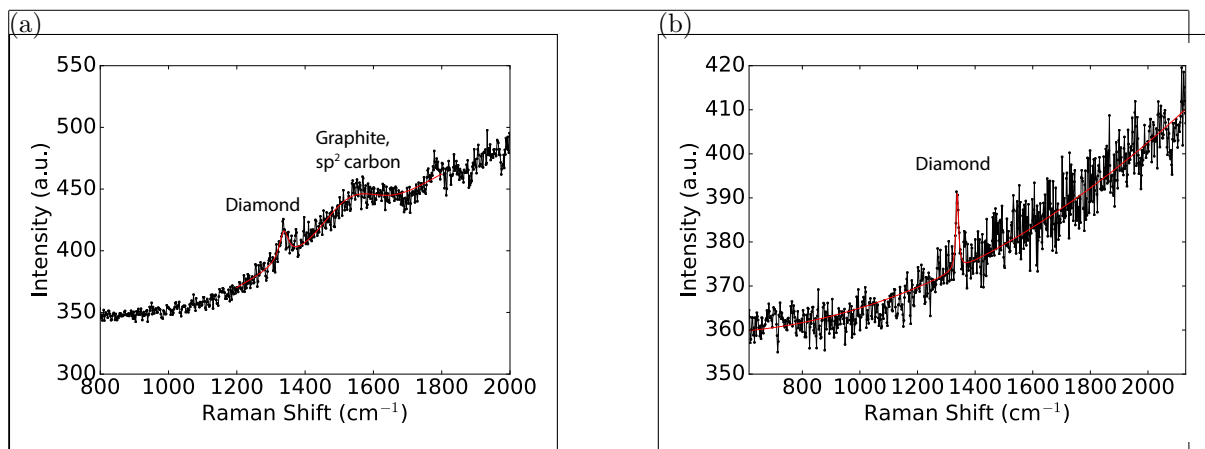


Figure 5.1: Raman measurements, black: data, red: fit. (a) Raman measurement before oxidation, sample insitu70. The diamond Raman peak is situated at  $1338\text{ cm}^{-1}$ . The broad feature around  $1600\text{ cm}^{-1}$  corresponds to the graphite G-band. (b) Raman measurement after oxidation, sample insitu70o. The G-band has vanished, indicating removal of graphite and amorphous  $\text{sp}^2$  hybridized carbon.

## 5.2 Raman Measurements

Raman measurements of the wet-milled nanodiamonds give insight to the issues of surface contamination, defects in the diamond lattice and strain in the lattice: Surface contamination like graphite and amorphous  $\text{sp}^2$  hybridized carbon atoms cause additional peaks in the Raman spectrum. A high defect concentration may lead to both additional peaks, to a broadening of the first order Raman peak and a shift to smaller wavenumbers. Strain in the diamond broadens the first order Raman peak and causes a shift to higher wavenumbers [23, 24, 25]. For the Raman measurements the same layout of the setup described in ?? is used. As excitation lightsource, a  $532\text{ nm}$  continuous wave diode laser is used (IO ). It provides single (frequency) mode laser light, which is a prerequisite for Raman investigations. The beam-splitter is a dichroic mirror (DRLP645), the laser light is additionally filtered out with a  $532\text{ nm}$  Notch filter in the detection path in front of the single mode fiber instead of the otherwise used longpass filter. With these adaptions, the combination of the confocal unit and the spectrometer serve as a Raman spectrometer. As the diamond Raman line is very narrow ( xx), the  $600\text{ grooves/mm}$  grating is used for a first overview; for more detailed measurements the  $1200\text{ grooves/mm}$  and  $1800\text{ grooves/mm}$  gratings are used.

Due to the low signal from a single nanodiamond, the Raman measurements are carried out at several areas on the sample insitu70 which are densely covered with nanodiamonds, hence taking measurements of clusters of nanodiamonds. The narrow peak in Figure 5.1a corresponds to the first order diamond Raman peak. The Raman shift of  $1338\text{ cm}^{-1}$  compared to the literature value of  $1332\text{ cm}^{-1}$  of pristine diamond [23] indicates the presence of strain in the diamond particles. Furthermore, the investigated Raman spectra show a broad peak with a Raman shift of about  $1582\text{ cm}^{-1}$  (Figure 5.1a). This shift corresponds to the G-band due to amorphous  $\text{sp}^2$  hybridized carbon atoms and graphite. The exact G-band position and linewidth is sensitive to parameters such as the clustering of the  $\text{sp}^2$  phase, bond-length and bond-angle disorder, presence of  $\text{sp}^2$  rings or chains, and the  $\text{sp}^2/\text{sp}^3$  ratio [26].

Nanodiamond Raman spectra are considerably modified after oxidation in air at  $450^\circ\text{C}$ . To

type

check  
number

verify this, we perform Raman measurements on three different spots on a non-oxidized sample (insitu70), and for comparison on three different spots on a sample produced in the same process which is additionally oxidized. While the G-band peak is present in every measurement performed on the sample which was not oxidized, it is not present in any of the measurements performed after oxidation (Figure 5.1b), indicating successful removal of  $\text{sp}^2$  hybridized carbon and surface graphite. The position of the diamond Raman peak is the same oxidized (insitu70o) and non-oxidized (insitu70n) samples, indicating no effect on strain in the diamond. On the other hand, the width of the diamond Raman peak is between  $15\text{ cm}^{-1}$  and  $30\text{ cm}^{-1}$  without oxidation treatment, but is only  $9\text{ cm}^{-1}$  to  $11\text{ cm}^{-1}$  after the oxidation process. A possible reason for a change of the width is improved crystal quality. This effect is also subject in the following paragraphs and will be explained in more detail there.

For comparison, measurements of the Raman line were also carried out on the implanted sample implanted250ao. These diamond particles are big enough to perform measurements on single nanodiamonds. We found one diamond Raman line at  $(1308 \pm 5)\text{ cm}^{-1}$ , one at  $(1345 \pm 5)\text{ cm}^{-1}$  and one at  $(1348 \pm 5)\text{ cm}^{-1}$  (given uncertainties are governed by spectrometer resolution). We have to distinguish two cases, a shift of the first order Raman line to higher versus lower wavenumbers than the first order Raman line of  $1332\text{ cm}^{-1}$  in pristine diamond.

As mentioned before, a Raman shift of the first order Raman line to lower wavenumbers and a broadening of the Raman line indicates defects in the diamond lattice [24]. The Raman line at  $(1308 \pm 5)\text{ cm}^{-1}$  exhibits a broad linewidth of  $(25 \pm 5)\text{ cm}^{-1}$ . Therefore both the position and the linewidth of the Raman line indicate that there are many defects present in the diamond. The other case is a shift of the first order Raman line towards higher wavenumbers. The shift of the first order Raman line to higher wavenumbers is attributed to strain in the diamond lattice. While under hydrostatic pressure, the triply degenerate first order Raman peak remains degenerate, under uniaxial and more complex stress configurations (biaxial stress, shear stress etc.) mode splitting occurs [24]. As the measured peaks at wavenumbers higher than the wavenumber in pristine diamond are broad, we attribute these peaks to stress configurations other than hydrostatic stress, where the mode splitting manifests itself in a broadening of the peak due to limited spectrometer resolution.

To summarize, there are two cases, one where the first order Raman line hints at many defects present in the diamond lattice and the other that leads to the assumption that the stress configuration in the diamonds are uniaxial or more complicated stress configurations. In section 6.1 we will show that both of these assumptions fit nicely to the results from the measured photoluminescence spectra.

### 5.3 Transmission Electron Spectroscopy Measurements

We performed transmission electron microscopy (TEM) measurements to further investigate the crystal quality<sup>2</sup>. For those TEM measurements, we used the sample insitu100. Smaller nanodiamonds would have been too small for the carbon grid which serves as a sample holder in the TEM, and might have fallen through the grid and bigger particles would have been too big to be transmitted by the electron beam, making the imaging impossible. In Figure 5.2 there are TEM images, one of them exhibits a single diamond particle and the other is a close-up image of a crystal boundary. From Figure 5.2a it can be seen that the diamond

beginning  
new text

<sup>2</sup>TEM measurements performed by J. Schmauch, group of R. Birringer, Saarland University

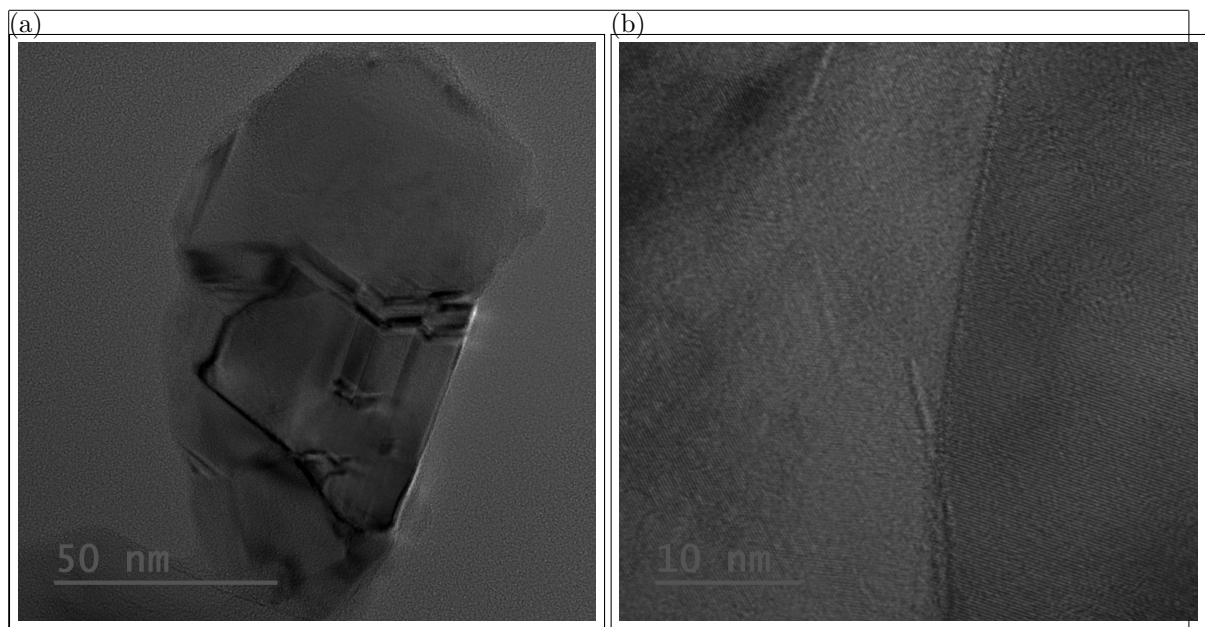


Figure 5.2: Transmission electron microscopy (TEM) pictures of sample insitu100. (a) Image of a single nanodiamond particle. Several crystal boundaries can be seen within the diamond particle. (b) Close-up image a diamond particle. The vertical line is a crystal boundary, to the left and right the more or less horizontal layers of one crystalline region can be seen.

particle contains several crystallites and crystal boundaries. The edges of the crystallites are the sharp features within the diamond particle, the crystal boundaries the smoother features. In Figure 5.2b the crystal layers which are more or less horizontal and in more or less the middle of the picture there is a vertical line which is the edge of a crystallite. So it is clear that the investigated sample does not contain beautiful single crystal diamond particles, which means a reduction of the crystal quality of the diamond particles.

er nur  
vermu-  
tung

end new  
text

---

---

## Chapter 6

# Spectral Distribution of SiV centers in Nanodiamonds

In the following chapter, spectroscopic measurements of the SiV centers are described. At first, a short introduction will be given. The additional theory, which goes beyond the scope of the explained theory in ?? and additional experimental equipment will be explained.

Throughout the work on this thesis, many different nanodiamond samples were investigated. While the ideal SiV center in unstrained bulk diamond has a linewidth of about 4 nm to 5 nm at a center wavelength of 738 nm at room temperature, it was observed that the center wavelength of the SiV center in nanodiamond varies []. At some point, it was thought that chromium centers are responsible for some of those shifted lines. With all the work performed on various nanodiamonds we can now say, that all the ZPLs we see are silicon related. It is possible that during *in-situ* growth atoms other than silicon are incorporated into the diamond lattice. In implanted high-purity diamond the possibility that the diamond contains color centers other than the implanted ones is very narrow. Therefore, we used implanted samples to confirm our findings we obtained with the *in-situ* implanted ones.

cite elke

### 6.1 Photoluminescence spectra

To find nanodiamonds containing SiV centers on the substrate, confocal scans are performed. The SiV centers are further investigated by measuring photoluminescence (PL) spectra, single photon statistics and photostability. To reduce bias in the measurements, not only the brightest spots are investigated, but also those which are hardly brighter than background fluorescence. The luminescence spectrum of an SiV center is composed of a prominent zero-phonon-line and weak sidebands. The ZPL is due to purely electronic transitions, whereas the sidebands are due to phonons either from vibrations of the color center or the diamond lattice. Investigations of both are reported independently in the following paragraphs.

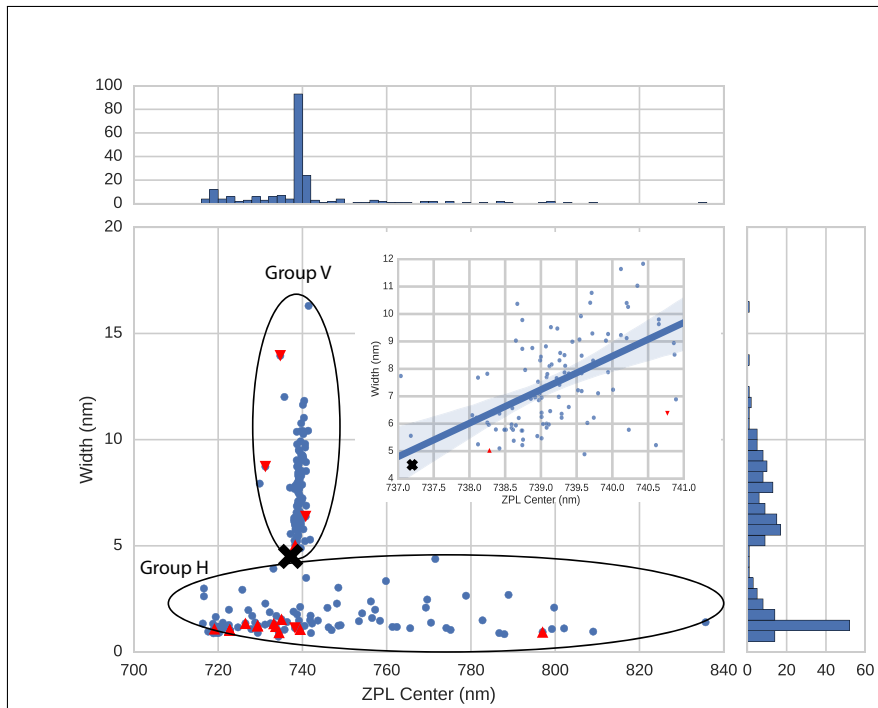


Figure 6.1: Distribution of the linewidth vs. the center wavelength of the ZPL of the investigated SiV centers in milled nanodiamonds containing *in-situ* incorporated SiV centers (samples insitu50, insitu70, insitu70n, insitu70o, insitu100). The data can be coarsely separated into two groups, H and V. The cross marks the position of an ideal SiV center in unstrained bulk diamond [1]. The red triangles indicate emitters which exhibited an antibunching dip in the  $g^{(2)}(0)$  measurement. Upwards pointing triangles represent emitters which exhibit fluorescence intermittency (blinking), while triangles pointing down represent emitters which do not exhibit any blinking (see section 6.3). The inset displays a zoom into group V, a least squares linear regression to the data, and the 95% confidence interval of the regression as a shaded area around the fit line. A clear trend of broader linewidths for longer ZPL center shifts is visible.

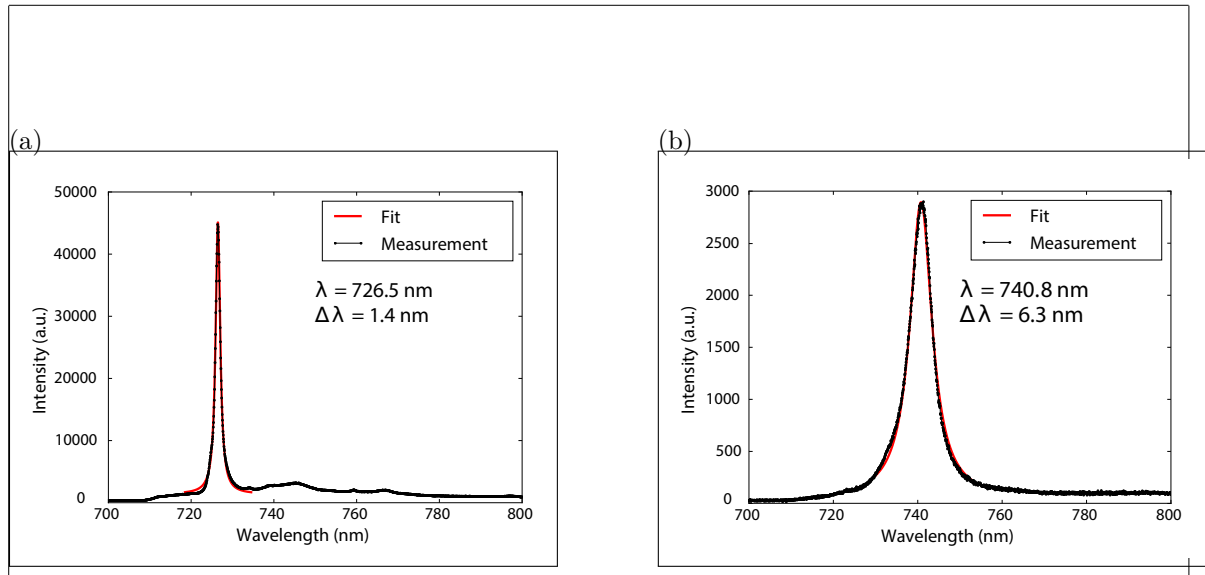


Figure 6.2: PL spectra measured with sample insitu100ao. (a) A representative room temperature spectrum of one of the emitters in group H of Figure 6.1, denoted emitter H1. (b) A representative room temperature spectrum of one of the emitters in group V of Figure 6.1, denoted emitter V1. The red lines are Lorentzian fits to the peaks.

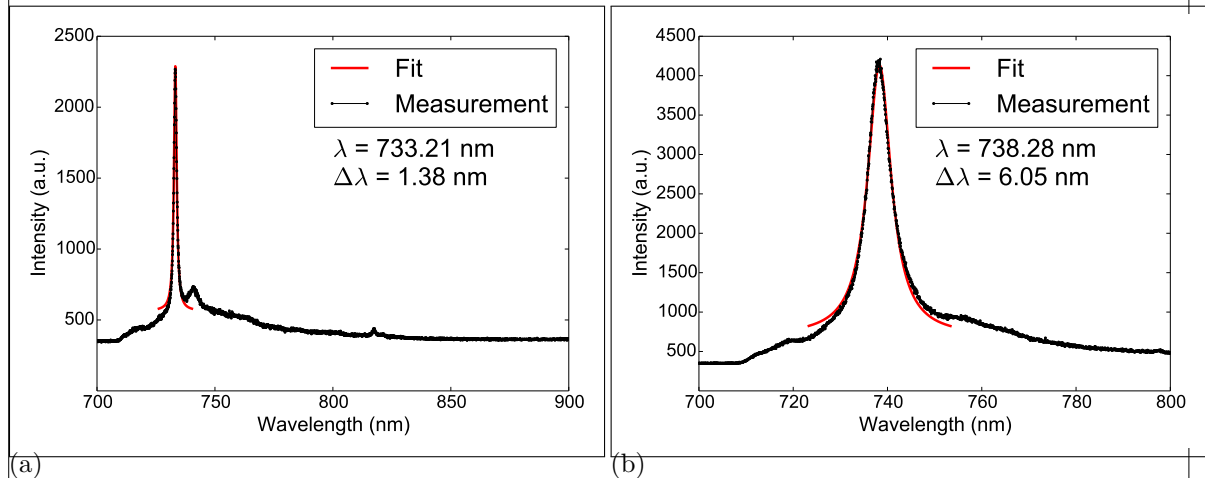


Figure 6.3: Other representative examples for a) a narrow (denoted emitter H2) and b) a broad (denoted emitter V2) ZPL. In contrast the spectra in Figure 6.2, the emitters depicted here exhibit stronger sidebands.

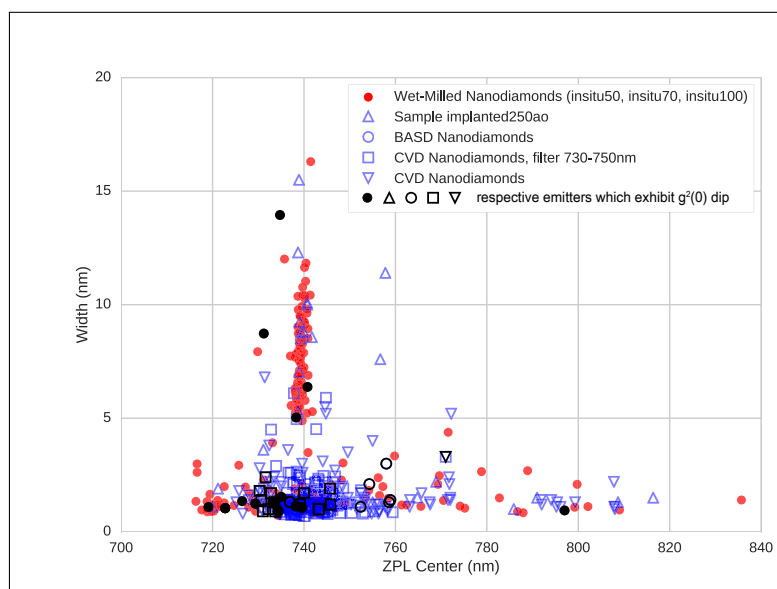


Figure 6.4: Comparison of the distribution of the linewidth vs. the center wavelength of the ZPL of the investigated SiV centers in milled nanodiamonds with data measured on the same nanodiamonds reported by J. Benedikter in [2], with data measured on CVD nanodiamonds, with data measured in CVD diamonds by E. Neu in a filter window between 730 nm and 750 nm [3], and with data measured on implanted250ao, implanted with Silicon. Black symbols represent emitters exhibiting a dip in the  $g^{(2)}(0)$  function, indicating a single or very few SiV centers

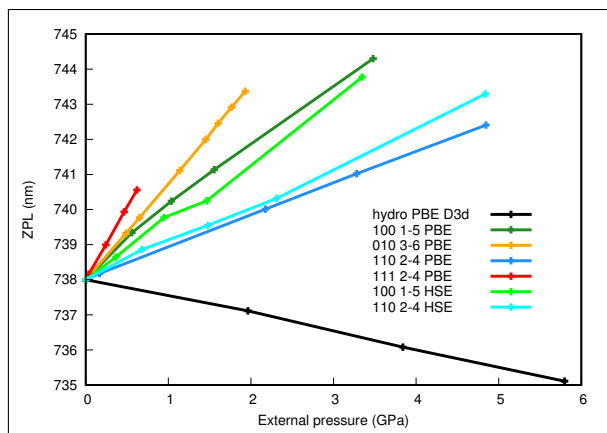


Figure 6.5: Calculations of the wavelength of the SiV center ZPL in dependence of pressure. Black: hydrostatic pressure; other colors: uniaxial pressure, for different orientations and calculated with different functionals PBE and HSE. Hydrostatic-type pressure causes a moderate blue shift whereas uniaxial strain causes larger redshift with different magnitudes depending on the direction of the strain better description from Adam Gali

### 6.1.1 Zero-phonon-line

The center wavelength and the linewidth of the zero-phonon-line of each measured SiV luminescence spectrum of the samples insitu50, insitu70, and insitu100 are determined by fitting a Lorentzian fit to the ZPL. Both spectra from single and multiple SiV centers are taken into account. The linewidth of each ZPL is plotted against its center wavelength (Figure 6.1). What immediately strikes the eye is a pattern that to our knowledge has not been reported to date: The observed ZPLs accumulate in two different regimes, namely a horizontal lobe (denoted group H) and a vertical lobe (group V) divided by a gap with hardly any data points. Single emitters are found both in group H and group V (for more details about single emitters see section ??).

The two groups are defined by their characteristic center wavelengths and linewidths: In group H very prominent ZPL peaks are found which show linewidths between about 1 nm to 5 nm at center wavelengths which vary between about 715 nm to 835 nm. Figure 6.2a shows a representative spectrum of a single emitter of group H (denoted emitter H1), exhibiting a ZPL line width of 1.4 nm at a center wavelength of 726.5 nm. In contrast, in group V, the spectra exhibit broader ZPL linewidths of about 5 nm up to 18 nm. Their ZPL center wavelengths, however, are distributed within a very narrow range between 738 nm to 741 nm. Figure 6.2b shows a spectrum of a single emitter of group V (denoted emitter V1), exhibiting a ZPL linewidth of 6.4 nm at a center wavelength of 740.8 nm. For comparison, the room temperature ZPL of SiV centers in unstrained bulk diamond shows a linewidth of 4 nm to 5 nm at a center wavelength of 737.2 nm marked with a cross in Figure 6.1 [1, 27].

We also investigated the Debye-Waller of the reported spectra, which states the amount of emission light stemming from the ZPL wrt. emission from sidebands. The Debye-Waller of emitter H1 amounts to  $0.81 \pm 0.01$ , corresponding to a Huang-Rhys factor of  $0.21 \pm 0.01$  which is in good agreement with the values reported in [28]. The error is mainly due to background correction. When zooming in to the spectrum of emitter V1 it shows, that it does not exhibit any sidebands, i.e. all emission goes into the ZPL. Considering resolution limits of the spectrometer, the Debye-Waller factor amounts to close to 100%. The signal-to-noise ratio in the chosen spectral window amounts to  $93\% \pm 1\%$ . It has to be pointed out, that we did not find any systematic difference of the Debye-Waller factor between group H and group V.

As the broad ZPL distribution shown in Figure 6.1 is unreported so far, we compare the results both to previous measurements and a control sample fabricated by silicon implantation. The comparison of current, earlier and control data is presented in Figure 6.4. Samples for which previous data has been taken are:

1. nanodiamonds produced by bead-assisted sonic disintegration (BASD) of polycrystalline CVD diamond films ([29]; data taken from [2])
2. nanodiamonds produced directly via a CVD process with *in-situ* incorporated SiV centers; measured in a spectral filter window of 730 nm to 750 nm (data reused from [3] with permission)
3. nanodiamonds produced in the same manner as the sample above; spectroscopic measurement procedure the same as the one performed on the milled, *in-situ* implanted samples (see Table 4.2, insitu50 etc.)

All previous data from different nanodiamond material fit nicely with the ZPL distribution. To rule out that the two lobes in the distribution are no artifacts due to other elements incorporated into the nanodiamonds during the process, such as residue from other processes

performed in the growth chamber or material abrasion from chamber parts and to verify that the observed luminescent defects are indeed silicon related, we performed control experiments that were implanted with silicon to form SiV centers (sample implanted250ao). Figure 6.4 shows that the implanted SiV centers cover roughly the same spectral range as the grown-in centers, thereby providing strong evidence for the silicon related origin of the defects. In the next paragraphs, the ZPL distribution will be discussed in further detail. At first, the ZPL center wavelength shift is investigated. Very few of the measured data points in group V sit at a shorter center wavelength than the point attributed to an ideal SiV center in unstrained bulk material. This means, a red-shift of the ZPL of an SiV center is more likely than a blueshift. Several mechanisms contribute to the center wavelength shift, namely hydrostatic- and material strain. As explained in ??, we measured the Raman shift of samples insitu70 and implanted250ao. These measurements indicate strain in the diamond lattice. Figure 6.5 shows the calculated shift of the ZPL in dependence of pressure in the diamond lattice both for hydrostatic stress and for uniaxial stress. PBE and HSE are two different functionals used for the calculations . From Figure 6.5 it can be seen, the assumption stated in ?? that the strain in the nanodiamonds is mainly due to uniaxial stress corresponds well with the measured ZPL red-shift in group V. With higher uniaxial pressure, the ZPL becomes more and more red-shifted. However, the measured shifts in group H are too broad to be solely explained by strain in the diamond. We suspect that there are other defect sites present in the vicinity of the SiV center which explain the strong variation [30]. This statement is strengthened by the measurement of the shift of the first order Raman peak to lower wavenumbers. The investigation of this hypothesis presents an interesting topic for further research.

Zooming in to group V, another effect becomes visible (inset in Figure 6.1): With increasing ZPL, the linewidth becomes broader. The data points in group V are fitted with a linear regression to guide to the eye. Linking the correspondence between the strain and the red-shift of the ZPL with that of the slope of between the center wavelength of the ZPL and the linewidth leads to the conclusion that also the linewidth is affected by strain in the diamond lattice: The higher the uniaxial stress, the bigger the linewidth.

To conclude, we are able to explain group V very consistently with theoretical predictions for the ZPL center wavelength shift due to strain in the diamond lattice. On the other hand, we suspect that group H is due to lattice defects in the vicinity of the SiV center, which has to be investigated in further research.

### 6.1.2 Sideband

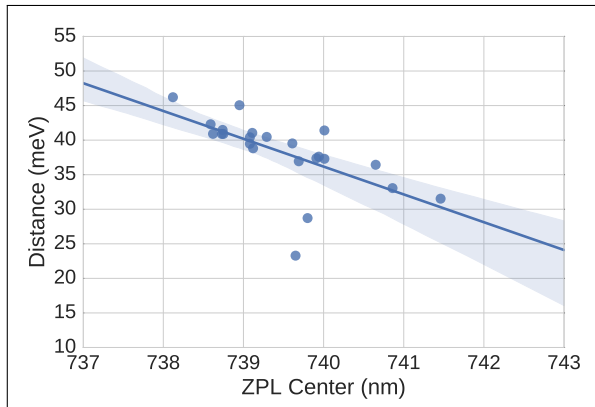
As mentioned before, phonons of the diamond lattice and the color center manifest themselves as peaks in the sideband of the photoluminescence spectrum. Phonons reduce the intensity of the the purely electronic transition, the zero-phonon-line. The electron-phonon coupling is quantified by the Debye-Waller factor or the Huang-Rhys. The former is the integrated intensity of the zero-phonon-line  $I_{ZPL}$  divided by the integrated intensity of the photoluminescence of the whole spectrum, i.e. ZPL plus sidebands,  $I_{tot}$  [7, ?]. The Huang-Rhys factor  $S$  is defined as  $I_{ZPL}/I_{tot} = \exp\{-S\}$ .

From literature it is known, that the SiV center in nanodiamond exhibits a large Debye-Waller of over 70% [31, 28], which is consistent with our measurements of emitter H1 and emitter V1. Nevertheless, sideband peaks are present in many SiV center PL emission spectra. The investigated emitters exhibit two different structures of sideband spectra: The spectra in group

input  
Adam  
Gali

beginning  
new

end new



V exhibit one strong sideband peak (Figure 6.7), spectra in group H exhibit several weaker sideband peaks.

However, there is no recurring pattern in the sideband of group H. The challenge arises to unequivocally distinguish between peaks stemming from a phonon sideband and peaks stemming from shifted, less intense SiV center ZPLs. The possibility exists, that some peaks identified as phonon sidebands are actually ZPLs stemming from shifted SiV centers. Therefore, we will focus our investigations on the more prominent sideband of group V.

Most of the spectra in group V exhibit a characteristic shape, composed of the ZPL and one strong sideband peak which is mostly shifted 37 meV to 43 meV. In reference [27] the 42 meV sideband peak is attributed to a non-localized (lattice) mode. It is also stated, that the local vibrational mode at 64 meV is much stronger than the 42 meV sideband peak. While the peak attributed to the non-localized mode is very strong in our measurements, we cannot identify the peak attributed to the local vibrational SiV center mode in the spectra of group V. A possible explanation is, that the lattice mode at 37 meV to 43 meV is so strong that the local vibrational mode at 64 meV cannot be separated from the tail of the lattice mode. In Figure 6.6 the distance between the center wavelength of the sideband peak and the center wavelength of the ZPL is plotted against the ZPL center wavelength. The distribution is fitted with a linear regression. We attribute the variance in the sideband shift to strain:

**Adam Galis Erkenntnisse**

For further investigations, we plotted the ZPL of group V with multiple peaks. We found that two Lorentzian fits fit the peak best. Figure 6.8 shows histograms of the distribution of the continuous wave and the linewidth of the fitted peaks. Keep in mind that two of the peaks sum up to the peak visible as a ZPL and the third peak is the sideband peak which we attribute to a lattice mode. We found that the linewidth of the sideband peak exhibits values up to 20 nm. This broad width is an indicator, that the local vibrational mode might indeed be outpowered by the more intense lattice mode. However, it is not very easy to find spectra where the sideband peak is pronounced and isolated enough to make proper statistics. The original ZPL is split up in two peaks, one with a median center wavelength of 738 nm and a median linewidth of 4.5 nm and the other with a median center wavelength of 742 nm and a median linewidth of 8 nm. It could be that this is an indication for another sideband peak at 742 nm. This assumption could be verified by cryostatic measurements, where the phonon sideband should vanish and only the ZPL survive and split up into the four-level fine structure.

beginning  
new

correct  
and verify all  
numbers

end new

### 6.1.3 Cryostatic Measurements

We performed some cryostatic measurements to pursue two goals: First, if we see the four-level splitting of the ZPL this is further proof that the dominant peaks of our spectra are indeed all due to SiV centers and do not stem from other impurities. Second, if the sideband peaks vanish at cold temperatures, this is evidence that they are caused by phonons. So we cooled down a sample, but all we saw was a wood of lines. Apparently, there were multiple SiV centers in the nanodiamonds and they were all strained, messing up the four-level line structure.

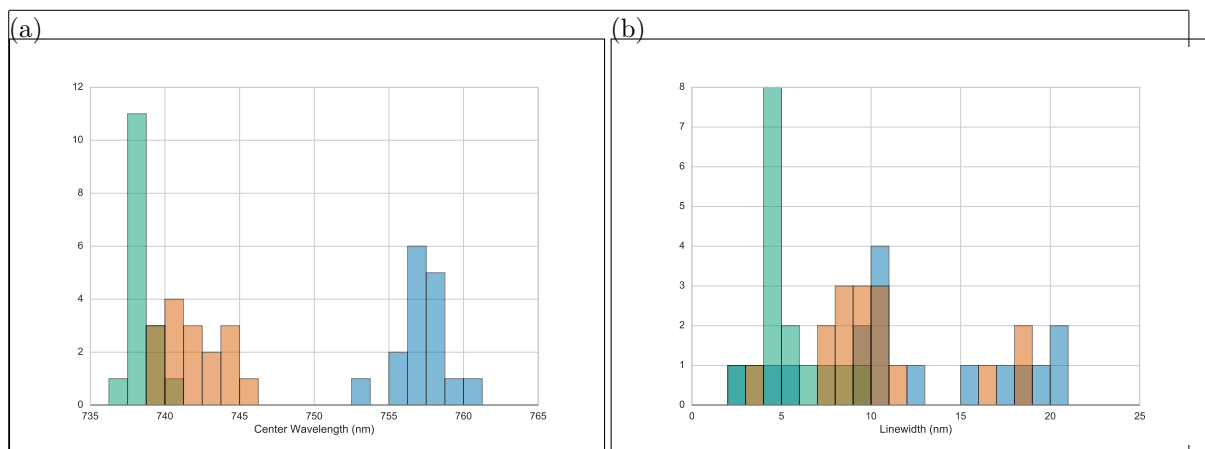


Figure 6.8

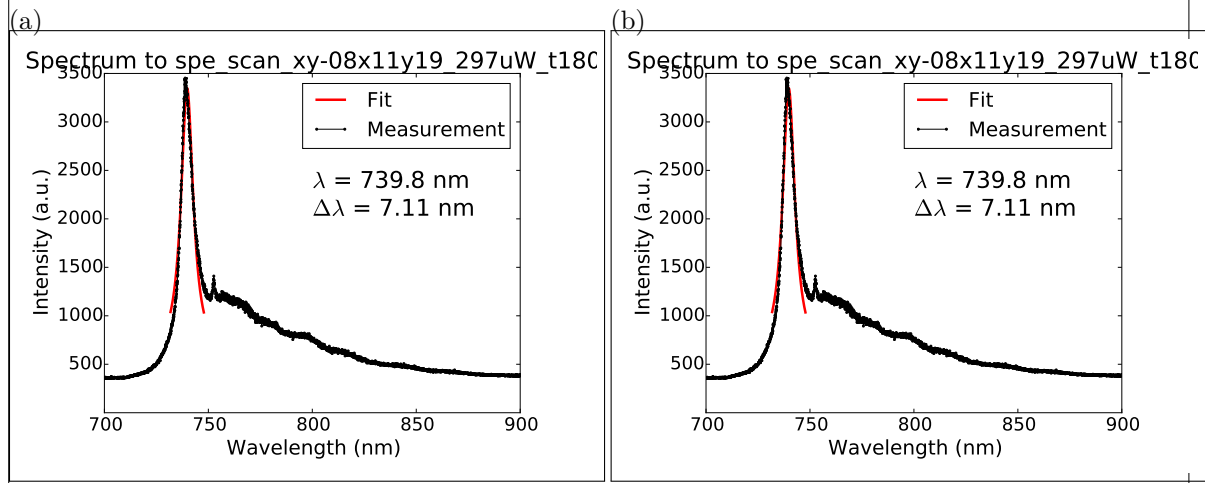


Figure 6.9

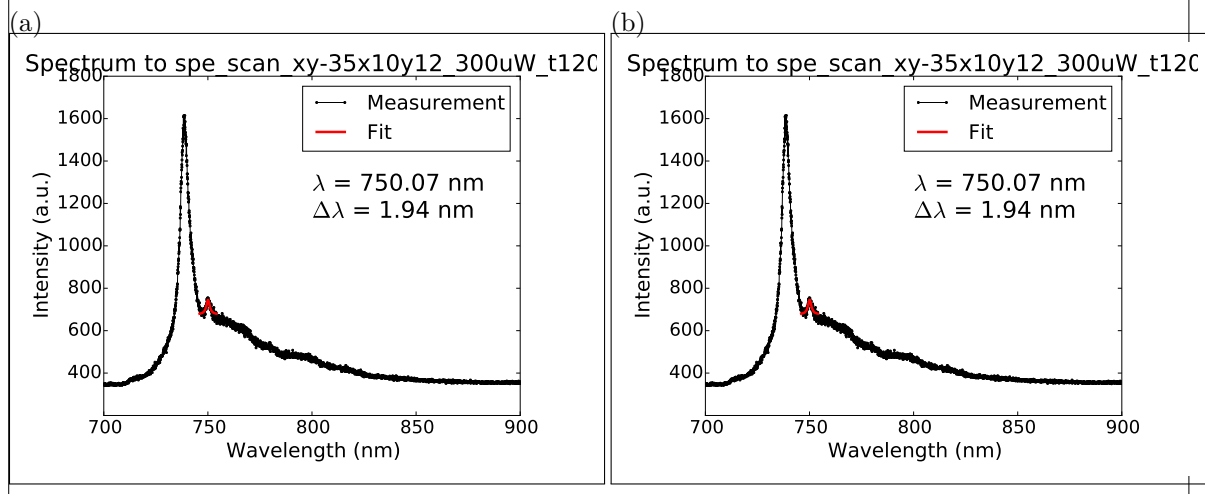


Figure 6.10

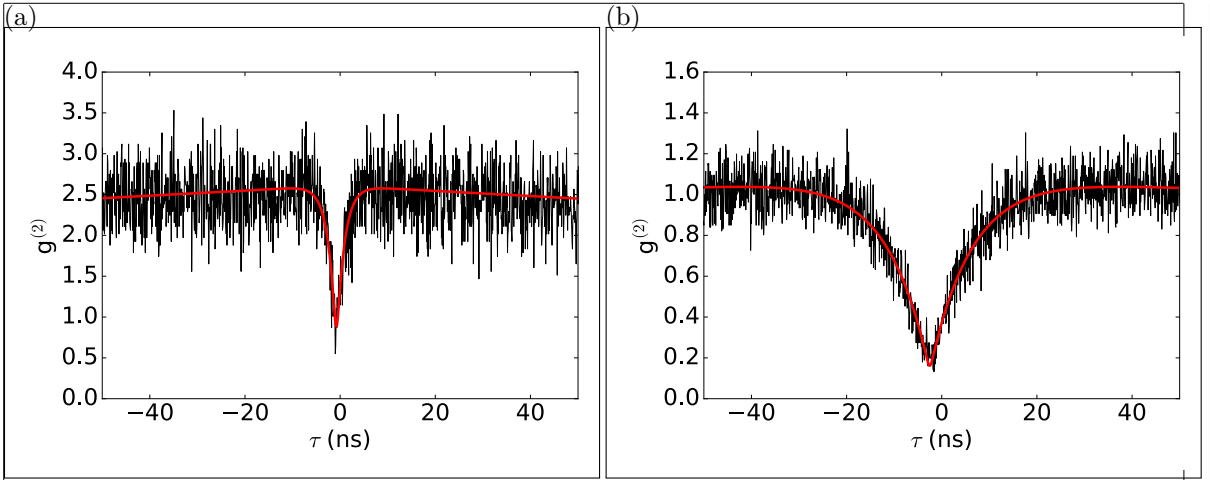


Figure 6.11: (a) Intensity autocorrelation function of emitter H1 at an excitation power of 15  $\mu\text{W}$ . (b) Intensity autocorrelation function of emitter V1 at an excitation power of 200  $\mu\text{W}$ , which is 25% of the saturation count rate.

## 6.2 Photon Statistics

The investigated SiV centers exhibit count rates of a few thousand to a few 100 000 cps. We carried out measurements of the photon statistics and found that about 3% of the SiV centers are single color centers. These measurements show, that the probability of finding a single emitter does not correlate in any way with the center wavelength of the ZPL or the linewidth of the ZPL. We found several single SiV centers with an antibunching dip down to about 0.2 and attribute the residual  $\bar{g}^{(2)}(0)$  value to background fluorescence from the diamond host. For the utilized nanodiamonds an of the background measurement independent of SiV center photoluminescence is impossible, because the laser spot size is bigger than the nanodiamond. Therefore, the SiV center will always be excited when the nanodiamond is illuminated. The measured lifetimes of the single SiV centers are in the range of 1 ns to 7 ns. Figure 6.11 shows the  $\bar{g}^{(2)}$  functions of the two emitters introduced in section 6.1, emitter H1 and emitter V1. Figure 6.11a shows the photon correlation function of emitter H1 at a power of 15  $\mu\text{W}$ . The fit of the data for an excitation power of 15  $\mu\text{W}$  yields a lifetime of the excited state of  $(1.6 \pm 0.1)$  ns. The  $\bar{g}^{(2)}(0)$  values of the same fit is 0.88, which corresponds to eight equally bright emitters. However, the  $\bar{g}^{(2)}(0)$  value is probably overestimated due to the fast dynamics of the emitter which cannot be fully resolved. Measurements of other SiV centers in group H yield  $\bar{g}^{(2)}(0)$  values down to 0.2.

Figure 6.11b shows the  $\bar{g}^{(2)}$  function of emitter V1 at an excitation power of 200  $\mu\text{W}$ , which is 25% of the saturation power of that emitter, which amounts to 1 mW. The  $\bar{g}^{(2)}(0)$  values for yields  $0.16 \pm 0.06$ , therefore being a representative  $\bar{g}^{(2)}$  measurement of single SiV centers. The fits yield a lifetime of the excited state of  $(6.3 \pm 0.2)$  ns. While it is not 0, it is well below 0.5, indicating single photon emission. The non-vanishing  $\bar{g}^{(2)}(0)$  value is caused by background fluorescence of the diamond.

Several spectra contain multiple narrow distinct peaks at different ZPL center wavelengths. This circumstance is attributed to a nanodiamond containing more than one SiV center, each of which is subject to a different center wavelength shift. We choose narrow bandpass filters to perform independent measurements of each individual SiV center peak of such a

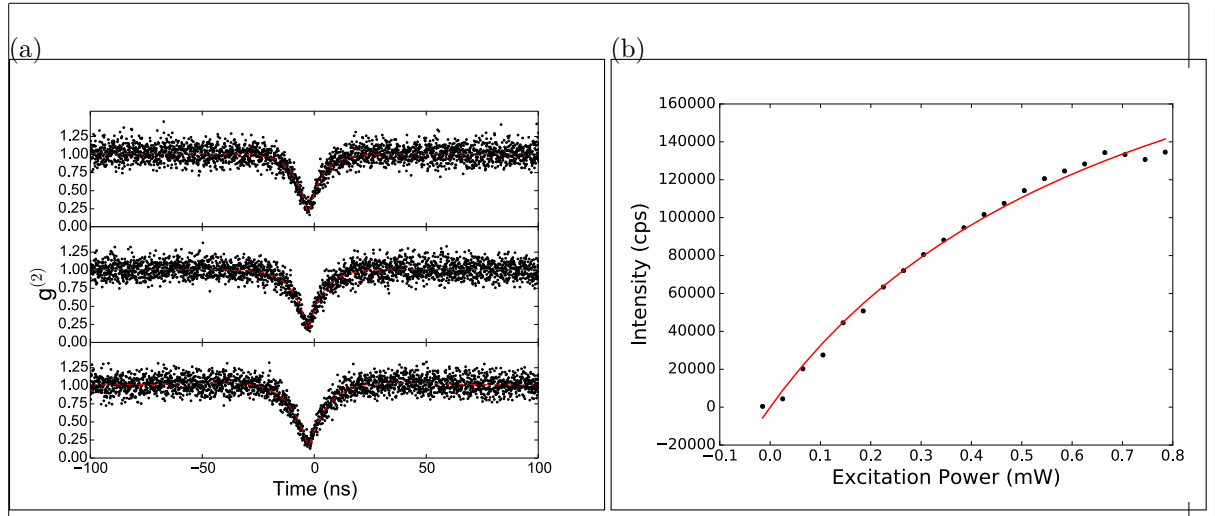


Figure 6.12: a) The  $g^{(2)}$  function of emitter xx at an excitation power of 200  $\mu\text{W}$ , 400  $\mu\text{W}$  and 500  $\mu\text{W}$  from bottom to top. b) Saturation measurement of the same emitter.

spectrum. Therefore it is possible to measure  $g^{(2)}(0)$  values below 0.5 for each of those narrow peaks. Hence the individual peaks are identified as single emitters with a different ZPL center wavelength.

Due to fast dynamics of the SiV center and the limited timing resolution of the APDs in the experimental setup (overall resolution of  $\sim$ 700 ps) it is not possible to fully resolve the narrow antibunching dip down to lower  $g^{(2)}(0)$  values. The fit yields a lifetime of the excited state of 710(30) ps at an excitation power of 500  $\mu\text{W}$ .

think of  
emitter  
names

## 6.3 Photostability

As mentioned in the previous section, the investigated SiV centers exhibit count rates of a few thousand to a few 100 000 cps. To further investigate the count rate, the luminescence time trajectory of the emitters which exhibit a dip at  $g^{(2)}(0)$  is evaluated. It is found that some of the observed emitters exhibit fluorescence intermittence, also called blinking (Figure 6.16). Blinking is attributed to temporal ionization of the color center during optical excitation, forming an optically inactive charge state [32, 21, 33]. Therefore the emitters change between states of higher and lower emission, i.e. brighter and darker states, called blinking levels.

The time trace of the emitter is shown in Figure 6.16. In the overview picture (Figure 6.16a), a few blinking dips can be seen with retention times of up to a few minutes. The fact, that the count rate never drops to the dark count rate lets us assume, that there are at least two SiV centers present, one exhibiting fluorescence intermittence and one exhibiting a stable emission. When zooming in, shorter retention times are observable (Figure 6.16b). The retention times range from a few tens of milliseconds up to a few seconds with a few outliers exhibiting very long retention times up to a few hundred seconds.

The retention times of the bright and of the dark state exhibit different probability distri-

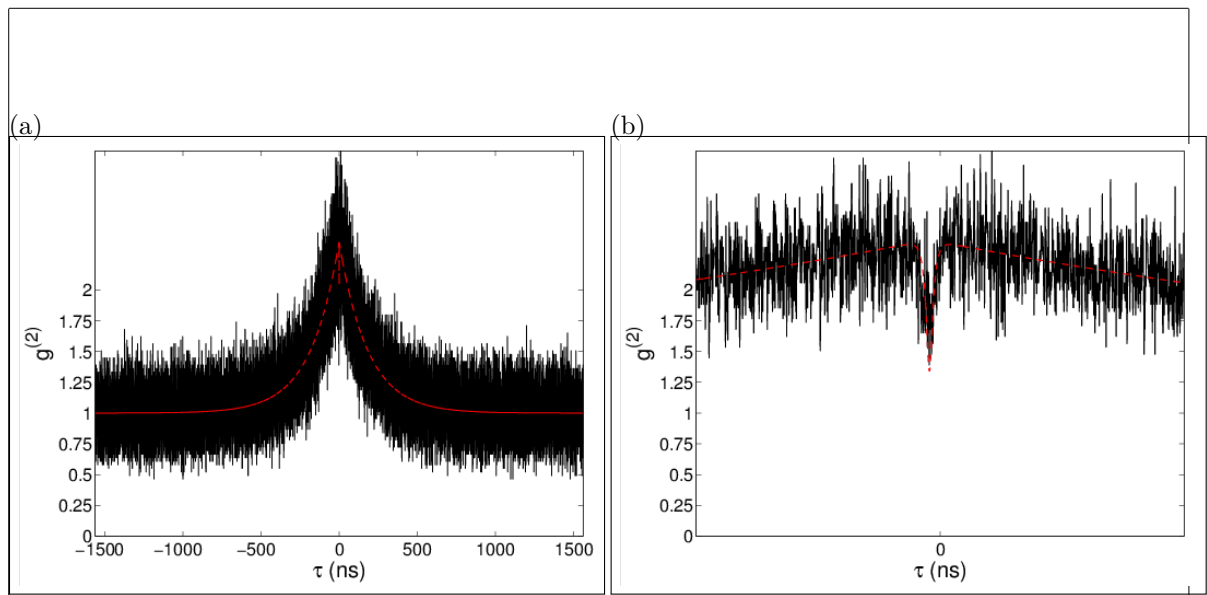


Figure 6.13: Photon autocorrelation measurement of emitter **xx** at an excitation power of 500  $\mu\text{W}$ . a) It is evident, that it exhibits a strong bunching. b) In a detail image a small antibunching dip can be seen. While it can be fit with the fitting function of a single emitter, the dip probably does not get fully resolved due to fast dynamics.

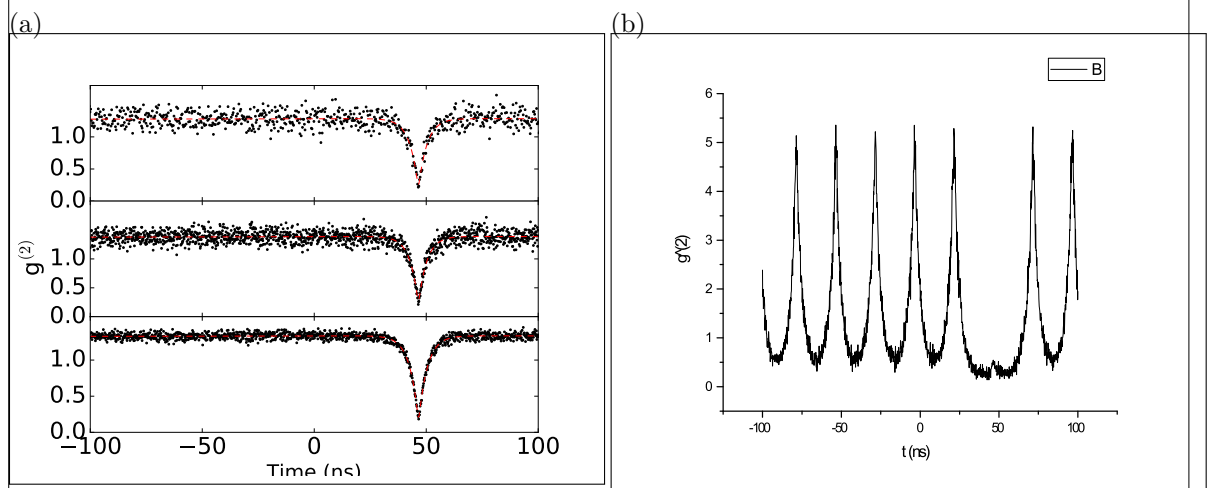


Figure 6.14:  $g^{(2)}(0)$  measurements of emitter **xx** a) power-dependent, continuous excitation, b) pulsed excitation

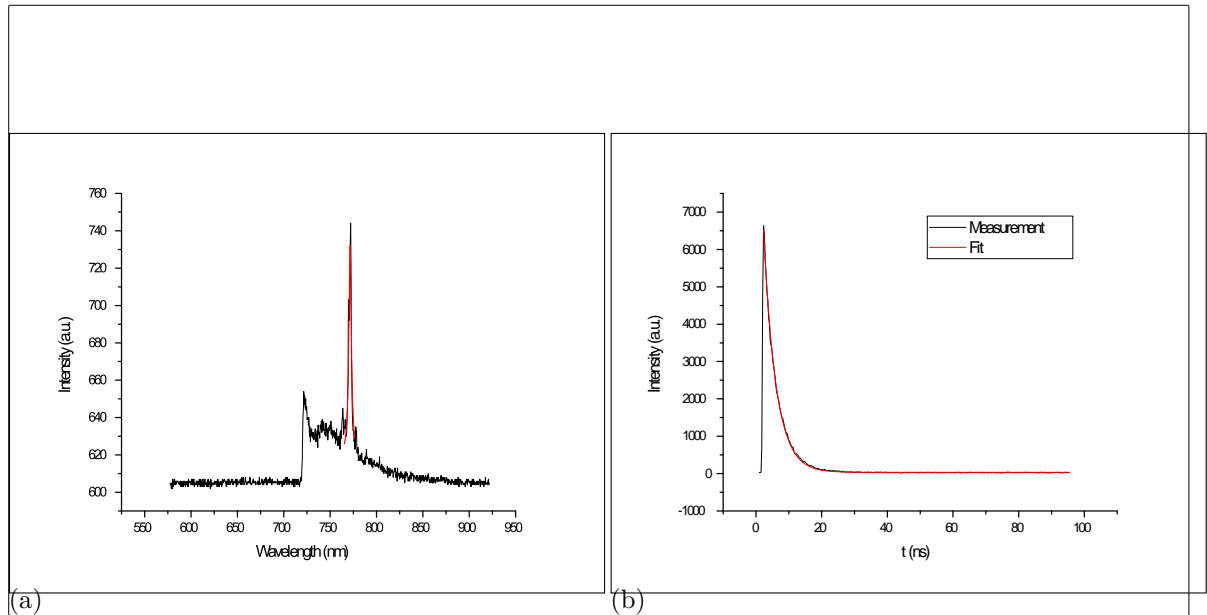


Figure 6.15: a) Spectrum of emitter **xx** b) lifetime measurement of emitter **xx**

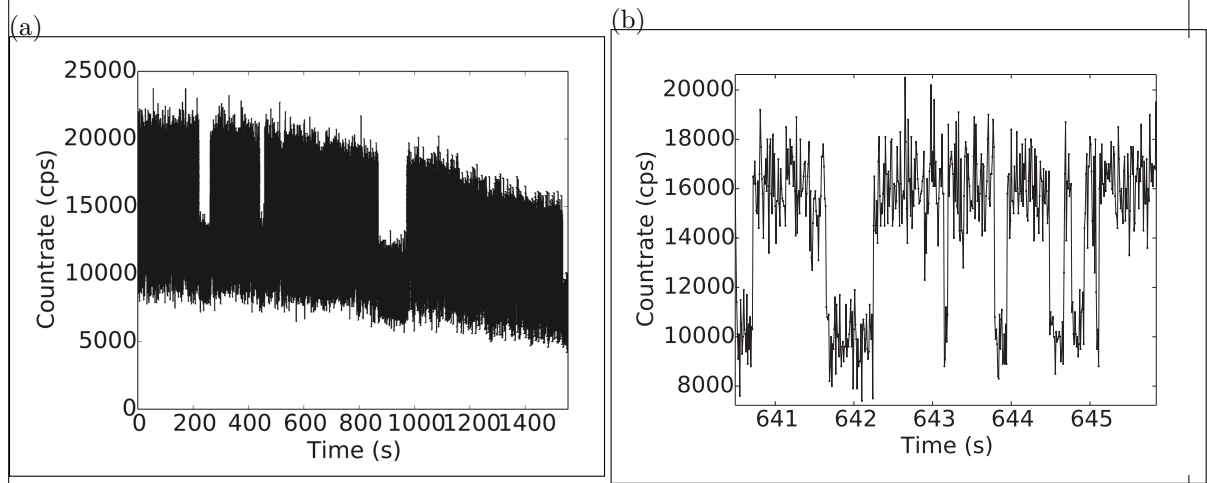


Figure 6.16: Distribution of countrate of a blinking level vs. its retention time in this level. (a) Time trace of the single emitter exhibiting the highest blinking rate. The variation of the countrate in the upper state is attributed to a drift of the setup. (b) Detail of the time trace of the same emitter.

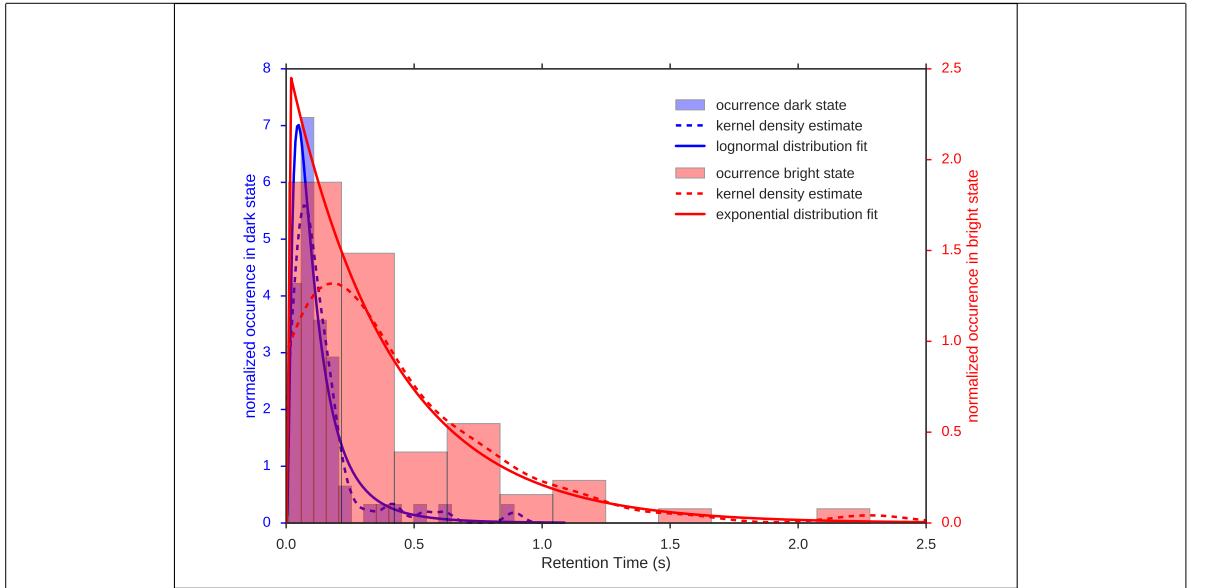


Figure 6.17: Retention times of the single emitter exhibiting the highest blinking rate in the bright (red) and dark (blue) states. The dashed line represents a kernel density estimation of the distribution of retention times. The y-axis is scaled to the normalized kernel density estimate. The red solid line is an exponential fit of the bright state retention times, the blue solid line is a lognormal fit of the dark state retention times. The fits are in good agreement with the data (p-values: red 0.92, blue 0.77)

bution functions and with that, different characteristic retention times. The red histogram in Figure 6.17 shows the retention times of the emitter in the bright state, whereas the blue histogram shows the retention times of the dark states (both omitting outliers with very long retention times). The dashed lines are kernel density estimators of the distribution of the respective retention times (i.e. every data point is represented with a Gaussian function and the resulting functions are added up to model the whole data). The red solid line is an exponential fit of the distribution of retention times in the bright state. The high p-value of 0.92 confirms the goodness of the fit. The mean and the median retention time in the bright state obtained by the exponential fit amount to  $(0.13 \pm 0.13)$  s and 0.09 s, respectively. While other literature about solid state quantum emitters reports an exponential probability distribution for both retention times in bright and dark states[34, 35], we found a lognormal probability distribution for the retention time in the dark state. The solid blue line in Figure 6.17 is a lognormal fit of the distribution of the retention times in the dark state. With a p-value of 0.77 it is by far the best model to describe the data distribution. For comparison: The p-value of an exponential fit only amounts to 0.36. The median retention time in the dark state obtained by the lognormal fit amounts to 0.10 s, therefore being a bit longer than the median retention time in the bright state (neglecting very long retention times which are treated as outliers).

We do not identify a correlation between the count rate of a blinking level and its retention time. However, there is a correlation between the position in the bimodal distribution and blinking: All but one emitters in group H exhibit blinking, where only one of the emitters in group V exhibits blinking (Figure 6.1). This dependency suggests that emitters in strained nanodiamonds are more likely to exhibit blinking.

We explain the observed blinking as a manifestation of the local crystal disorder due to dislocations and impurities which act as a trap for the excited electron and therefore switching the emitter to the dark state [34]. The assumption that dislocations and impurities are responsible for blinking emitters is in agreement with our findings in ??, where we attribute the Raman line at wavenumbers lower than the value of pristine diamond to damage of the diamond lattice.

---

---

## **Chapter 7**

## **discussion**

---

---

## **Chapter 8**

# **Conclusion**

In conclusion...

---

---

## **Appendix A**

### **Text of Minor Interest**

Some data

# Bibliography

- [1] Carsten Arend, Jonas Nils Becker, Hadwig Sternschulte, Doris Steinmüller-Nethl, and Christoph Becher. Photoluminescence excitation and spectral hole burning spectroscopy of silicon vacancy centers in diamond. *Physical Review B*, 94(4):045203, jul 2016. iv, 37, 40
- [2] Julia Benedikter, Hanno Kaupp, Thomas Hügger, Yuejiang Liang, Alexander Bommer, Christoph Becher, Anke Krueger, Jason M. Smith, Theodor W. Hänsch, and David Hunger. Cavity-Enhanced Single-Photon Source Based on the Silicon-Vacancy Center in Diamond. *Physical Review Applied*, 7(2):024031, 2017. iv, 39, 40
- [3] Elke Katja Neu. *Silicon vacancy color centers in chemical vapor deposition diamond : new insights into promising solid state single photon sources*. PhD thesis, 2012. iv, 39, 40
- [4] J Y Cheung, C J Chunnillall, E R Woolliams, N P Fox, J R Mountford, J Wang, and P J Thomas. The quantum candela: a re-definition of the standard units for optical radiation. *Journal of Modern Optics*, 54(2-3):373–396, jan 2007. 1, 2
- [5] Current definitions of the SI units. 1
- [6] Joanne C Zwinkels, Erkki Ikonen, Nigel P Fox, Gerhard Ulm, and Maria Luisa Rastello. Photometry, radiometry and ‘the candela’: evolution in the classical and quantum world. *Metrologia*, 47(5):R15–R32, oct 2010. 2
- [7] Elke Neu. Woodhead Publishing Online - T&Cs January 2011. Number January. 2014. 2, 41
- [8] Charles. Santori, David. Fattal, and Yoshihisa. Yamamoto. *Single-photon devices and applications*. Wiley-VCH, 2010. 18
- [9] Mark (Anthony Mark) Fox. *Quantum optics : an introduction*. Oxford University Press, 2006. 19
- [10] Richard D. Younger, K. Alex McIntosh, Joseph W. Chludzinski, Douglas C. Oakley, Leonard J. Mahoney, Joseph E. Funk, Joseph P. Donnelly, and S. Verghese. Crosstalk analysis of integrated Geiger-mode avalanche photodiode focal plane arrays. *Advanced Photon Counting Techniques III*, 7320:73200Q1–12, 2009. 20
- [11] R F Davis. *Diamond Films and Coatings: Development, Properties, and Applications*. Hébert, Alexandre-Martin-Stanislas. Noyes Pub., 1993. 21
- [12] K H O'Donovan. Synthetic diamond. 21

- [13] Valery a. Davydov, a. V. Rakhmanina, S. G. Lyapin, I. D. Il'ichev, K. N. Boldyrev, a. a. Shiryaev, and Viatcheslav N. Agafonov. Production of nano- and microdiamonds with Si-V and N-V luminescent centers at high pressures in systems based on mixtures of hydrocarbon and fluorocarbon compounds. *JETP Letters*, 99(10):585–589, 2014. 22
- [14] John W. Arblaster. Crystallographic Properties of Iridium. *Platinum Metals Review*, 54(2):93–102, 2010. 22
- [15] S. Gsell, M. Fischer, R. Brescia, M. Schreck, P. Huber, F. Bayer, B. Stritzker, and D. G. Schlom. Reduction of mosaic spread using iridium interlayers: A route to improved oxide heteroepitaxy on silicon. *Applied Physics Letters*, 91(6):061501, aug 2007. 22
- [16] Robert F. Davis, editor. *Diamond Films and Coatings*. Noyes Pub., 1993. 22
- [17] S. Gsell, T. Bauer, J. Goldfuß, M. Schreck, and B. Stritzker. A route to diamond wafers by epitaxial deposition on silicon via iridium/yttria-stabilized zirconia buffer layers. *Applied Physics Letters*, 84(22):4541, may 2004. 23
- [18] Matthias Schreck, Jes Asmussen, Shinichi Shikata, Jean-Charles Arnault, and Naoji Fujimori. Large-area high-quality single crystal diamond. *MRS Bulletin*, 39(06):504–510, jun 2014. 23
- [19] Oliver A. Williams and Milos Český Nesládek. Growth and properties of nanocrystalline diamond films. *Phys. status solidi*, 203(13):3375–3386, oct 2006. 25
- [20] Peter Zapol, Michael Sternberg, Larry Curtiss, Thomas Frauenheim, and Dieter Gruen. Tight-binding molecular-dynamics simulation of impurities in ultrananocrystalline diamond grain boundaries. *Physical Review B*, 65(4):045403, 2001. 26
- [21] Elke Neu, Mario Agio, and Christoph Becher. Photophysics of single silicon vacancy centers in diamond: implications for single photon emission. *Optics Express*, 20:19956–19971, jul 2012. 26, 29, 46
- [22] M. S. Dresselhaus and R. Kalish. *Ion Implantation in Diamond, Graphite and Related Materials*, volume 22 of *Springer Series in Materials Science*. Springer Berlin Heidelberg, Berlin, Heidelberg, 1992. 32
- [23] AM Zaitsev. *Optical properties of diamond: a data handbook*. 2001. 33
- [24] Steven Prawer and Robert J Nemanich. Raman spectroscopy of diamond and doped diamond. *Philosophical Transactions of the Royal Society A: Mathematical, Physical and Engineering Sciences*, 362(1824):2537–2565, nov 2004. 33, 34
- [25] J. O. Orwa, K. W. Nugent, D. N. Jamieson, and S. Prawer. Raman investigation of damage caused by deep ion implantation in diamond. *Physical Review B - Condensed Matter and Materials Physics*, 62(9):5461–5472, sep 2000. 33
- [26] Andrea Carlo Ferrari and John Robertson. Raman spectroscopy of amorphous, nanosstructured, diamond-like carbon, and nanodiamond. *Philosophical Transactions of the Royal Society of London A: Mathematical, Physical and Engineering Sciences*, 362(1824):2477–2512, 2004. 33
- [27] Andreas Dietrich, Kay D Jahnke, Jan M Binder, Tokuyuki Teraji, Junichi Isoya, Lachlan J Rogers, and Fedor Jelezko. Isotopically varying spectral features of silicon-vacancy in diamond. *New J. Phys.*, 16(11):113019, nov 2014. 40, 43

- [28] Elke Neu, David Steinmetz, Janine Riedrich-Möller, Stefan Gsell, Martin Fischer, Matthias Schreck, and Christoph Becher. Single photon emission from silicon-vacancy colour centres in chemical vapour deposition nano-diamonds on iridium. *New Journal of Physics*, 13(2):25012, feb 2011. 40, 41
- [29] E. Neu, Carsten Arend, E. Gross, F. Guldner, C. Hepp, D. Steinmetz, E. Zscherpel, S. Ghodbane, H. Sternschulte, D. Steinmüller-Nethl, Y. Liang, A. Krueger, Christoph Becher, Et Al., Et al., Et Al., and Et Al. Narrowband fluorescent nanodiamonds produced from chemical vapor deposition films. *Appl. Phys. Lett.*, 98(24):243107, jun 2011. 40
- [30] GergÅŠ Thiering and Adam Gali. Complexes of silicon, vacancy, and hydrogen in diamond: A density functional study. *Physical Review B*, 92(16):165203, oct 2015. 41
- [31] Elke Neu, Martin Fischer, Stefan Gsell, Matthias Schreck, and Christoph Becher. Fluorescence and polarization spectroscopy of single silicon vacancy centers in heteroepitaxial nanodiamonds on iridium. *Phys. Rev. B*, 84(20):205211, nov 2011. 41
- [32] Uwe Jantzen, Andrea B Kurz, Daniel S Rudnicki, Clemens Schäfermeier, Kay D Jahnke, Ulrik L Andersen, Valery A Davydov, Viatcheslav N Agafonov, Alexander Kubanek, Lachlan J Rogers, and Fedor Jelezko. Nanodiamonds carrying silicon-vacancy quantum emitters with almost lifetime-limited linewidths. *New Journal of Physics*, 18(7):073036, jul 2016. 46
- [33] Adam Gali and Jeronimo R. Maze. Ab initio study of the split silicon-vacancy defect in diamond: Electronic structure and related properties. *Physical Review B*, 88(23):235205, dec 2013. 46
- [34] C Bradac, T Gaebel, N Naidoo, M J Sellars, J Twamley, L J Brown, A S Barnard, T Plakhotnik, A V Zvyagin, and J R Rabeau. Observation and control of blinking nitrogen-vacancy centres in discrete nanodiamonds. *Nature nanotechnology*, 5(5):345–9, may 2010. 49, 50
- [35] Amanuel M. Berhane, Carlo Bradac, and Igor Aharonovich. Photoinduced blinking in a solid-state quantum system. *Physical Review B*, 96(4):041203, jul 2017. 49

---

---

# Index

$g^{(2)}$  function, 19

Hanbury Brown and Twiss, 16

Hanbury Brown and Twiss setup, **19**

photon autocorrelation function, 19